DFT Study of Copper-Nickel (111) Catalyst For Methane Dry Reforming

Ahmed Omran

DFT STUDY OF COPPER-NICKEL (111) CATALYST FOR METHANE DRY REFORMING

A Thesis

by

AHMED SHERIF ALI SHERIF OMRAN

Submitted to the Office of Graduate and Professional Studies of
Texas A&M University
in partial fulfillment of the requirements for the degree of

MASTER OF SCIENCE

Chair of Committee,	Nimir Elbashir
Committee Members,	Patrick Linke
	Hamid Parsaei
Head of Department,	Nazmul Karim

May 2019

Major Subject: Chemical Engineering

ABSTRACT

No one can deny that the increasing energy demand -due to world population booming- and climate change are two major challenges facing humanity in the current century. Climate change phenomenon is basically related to green house gases (GHGs) emissions which result in increasing temperature of earth. Among GHGs, CO_2 is the major contributor in global warming while CH_4 is considered a major energy source as the main component of natural gas. Dry reforming of methane (DRM) achieves utilization of both CO_2 with CH_4 by producing syngas which can be converted into valuable compounds. Thus, DRM is a currently a hot subject in both industrial catalysis and environmental research.

The applicability of DRM in industry is hindered by its high energy demand and coke formation on catalyst surface which leads to rapid catalyst deactivation. Nickel catalyst is well-known for an activity comparable to those of the expensive and abundant noble metals. However, pure Ni catalyst can suffer from severe coke formation at the elevated temperatures required for DRM reaction. To reduce coke formation, Ni-bimetallic catalysts are examined as they have shown reasonable activity and reduced carbon deposition. Several nickel-transition metals bimetallic catalysts showed their potential for coke resistance and improved activity. While the synergetic effects of Co-Ni-bimetallic catalyst is found to be due to its oxophilicty, Ni- Fe catalyst activity is attributed to redox system formation. However, Cu behavior of coke resistance and activity enhancement is still not well-defined at molecular level at the time of this study.

This study uses DFT (Density Functional Theory) computational methods to evaluate DRM reaction on Ni2Cu (111) bimetallic catalyst. The study will reveal how different species of elementary reactions are adsorbed on catalyst surface, explore the reaction mechanism and investigate the role of atomic oxygen as well as hydroxide species in carbon removal and catalyst stability in presence of Cu in the Ni-Ni network. The results will also explain the dominant reaction pathway by calculating the activation energy barriers of different elementary reactions and contribute to design of new stable and coke-resistant catalyst that can be used for DRM on the industrial scale.

DEDICATION

I kneel humbly to Allah, thanking HIM for showing me the right path, without HIS help my efforts would have gone in vain.

For my dear parents, thanks for everything, I would not be there without your kind support and prayers.

My wife Sahar, and my beloved Sherif and Mariam, who experienced all of the ups and downs of my research and support me all the time, thank you for the happiness you brought to my life.

For my sister, brothers, family and friends, thank you for your kind wishes, advice and support.

Last but not least, my deep than gratitude to my friend and colleague for 18 years Dr.Ahmed Hamid, thanks for your kind clues and support.

I dedicate this work to you all and promise that this is only a start.

Thank you!

ACKNOWLEDGEMENTS

I would like to thank my advisor, *Prof. Nimir Elbashir* for his kind support, from both personal and technical perspectives, and his guidance through all this work. I would like to extend my sincere gratitude for my committee members, *Prof.Patrick Linke* and *Prof.Hamid Parsaei*, for their guidance throughout the course of this work. The members of Office of Graduate and Professional Studies at Texas A&M University at Qatar are also sincerely acknowledged for their support.

I am especially grateful to *Dr. Minhaj Ghouri* for his support, helpful discussions and his assistance in running the computational campaign from scratch. My sincere thanks are extended to all members of our research team for their valuable scientific discussions and meetings. I am sincerely grateful to *Dr.Ahmed Abdel Wahab* for his early encouragement and support. I am greatly thankful TAMUQ Computational Research team, Prof. Othmane Bouhali and his team, who made it possible for me to have this thesis as well. In addition, I would like to express my deep gratitude to all the faculty and staff at the TAMUQ chemical engineering program for their valuable assistance and reviews. Moreover, I would like to express many thanks to *Prof.Gaber ElEnany* from Port Said University (PSU), without his kind support, I would not be here today. My sincere gratitude is extended to *Dr. Graeme Henkelman* from UTA and my fellow *Dr. Andrew Rosen* from Northwestern University for their valuable thoughts and help.

Finally, I would like to thank my friends and colleagues at TAMUQ for making my time here a lively experience.

CONTRIBUTORS AND FUNDING SOURCES

Contributors

This work was supervised by a thesis committee consisting of Professor *Nimir Elbashir* as advisor, Professor *Patrick Linke* of the Department of Chemical Engineering as well as Professor *Hamid Parsaei* of the Department of Mechanical Engineering.

The simulations in Chapter 4 were performed on the supercomputing clusters RAAD & RAAD2.The hardware & software (VASP™) support from TASC at TAMUQ is gratefully acknowledged .All other work conducted for the thesis was completed by the student independently.

Funding Sources

Graduate study was partially supported by Itochu fellowship from Chemical Engineering Department at Texas A&M University at Qatar.

This work was also made possible in part by NPRP award [NPRP X-100-2-024] from the Qatar National Research Fund, which is a member of the Qatar Foundation. Its contents are solely the responsibility of the authors and do not necessarily represent the official views of the awarding parties.

NOMENCLATURE

A	Pre-exponential factor
Al_2O_3	Alumina
cNEB	Climbing nudged elastic band method
DFT	Density functional theory
DRM	Dry reforming of methane
E_a	Activation Energy
FS	Final state
GHGs	Green house gas
hTST	Harmonic approximation of transition state theory
IS	Initial state
k	Rate constant
MEP	Minimum energy path
NEB	Nudged elastic band method
n(r)	Electron density
SMR	Steam reforming of methane
TST	Transition state theory
ν_i	Real frequency
ν'_i	Imaginary frequency
ZPE	Zero-Point energy correction

TABLE OF CONTENTS

Page

LIST OF FIGURES

Page

LIST OF TABLES

Page

1 INTRODUCTION AND LITERATURE REVIEW

1.1 Introduction

"***Let us face it, there is no Planet B***" said *Emanuel Macron*, the French president while he addressed the US lawmakers suggesting that U.S. should come back and rejoin the Paris Climate Agreement[1]. No doubt that increasing concern over global warming and greenhouse gases (**GHGs**) effect has been accelerated in the last decades. With estimated 25.7 gigatons emissions into our atmosphere, CO_2 can be considered a major contributor to global warming[2]. Despite the efforts from organization such as European Union, Fossil fuels still hold a major share in the energy mix that resulted from the increasing energy demand. Utilization of fossil fuels escalates the CO_2 emissions and worsens their global warming effect. Capturing CO_2 and using it as a chemical feedstock can be a double benefit for both environmental and profitability perspective that can drive lawmakers and industry towards more green economy[3,4].

Monetization of both CO_2 with CH_4, which is the most problematic greenhouse gas, into more valuable compounds is key subject in industrial catalysis and environmental research[5,6]. Fossil fuel consumption releases million tons of CO_2 and other (GHGs) into the atmosphere which is a main factor to global warming and climate change. Hansen et al showed that the temperature rose at least 0.8 ◦C since 1951 and have forecasted of continuous increment in 21st century[7]. Among the GHGs, while CO_2 is the most important contributor in terms of quantity emitted[8], natural gas that is mainly composed of methane and other light hydrocarbons C_2-C_4 is a major player as clean

energy resource. For the major natural gas producers such as USA, Qatar and Russia, methane monetization represents a major drive for the whole economy. For these countries, the approach utilization of both CO_2 and methane will not only save the environment[9,10], but also it will boost both local, regional and global economy[11]. In the context, dry reforming of methane that utilize both major GHGs, which is CH_4 and CO_2, is one of the attractive processes for converting the GHGs into value-added chemicals and fuels [12,13,14,15,16].

The Dry Reforming of Methane (DRM) reaction is given by the following equation:

$$CH_4 + CO_2 \rightarrow 2\,CO + 2H_2 \qquad \Delta H^{\circ} = 247.3\ kJ\ mol^{-1} \qquad 1)$$

The DRM reaction catalytically reform CH_4 with CO_2 to result in syngas (CO and H_2). In return, the produced syngas is very valuable precursor for many other products and uses. It can be used either directly as fuel or converted to other hydrocarbons to produce valuable and ultra-clean fuels and products such as methanol, diesel, gasoline, kerosene and naphtha through Fischer-Tropsch and other reactions[17,18,19,20] . Moreover, DRM can be used in other industries as in steel manufacturing where syngas plays the role of reducing agent to get reduced iron[21].

Despite the recent improvements and researches related to DRM, certain challenges are persistent and still required to be faced. First and foremost, the reaction is highly endothermic and energy intensive which limits the uses due to large capital required. The reaction need to be controlled above 700 °C otherwise competitive

reactions will dominate and enhance carbon formation. This coke formation itself is another major challenge as it causes rapid catalyst deactivation and results in less efficient non-stable reaction which hinders the industrial application. Thus, producing of stable and efficient catalysts with economic visibility is very crucial for long term operation[22]. Recently, the proposed solutions to address these challenges include combined reforming and optimization [23,24,12], and developing catalysts that resist coke formation[25,26].

1.2 Overview on Ni-based catalysts for DRM

Recent researches used different metal catalyst such as Platinum (Pt), Rhodium (Rh), Iridium (Ir), Cobalt (Co) and Nickel (Ni) for DRM. It cannot be denied that noble metals such as Ru and Rh proved their higher catalytic activity, prolonged stability as well as coke resistance. Pakhare and Spivey[22] reviewed the performance of different noble metals in DRM and investigated their effect on the reaction kinetics and mechanism. However, noble metals are costly and less abundant which limit their economic attractiveness for the large industrial scale use[22].On the opposite side, Ni-based catalysts showed comparable catalytic activity to noble metals, still it is a cheap alterative transition metal with high availability[27,28,29].

Catalyst design and synthesis play a major role in the catalytic performance. Properties such as strong metal-support interaction, dispersion and size, oxygen storage capacity, basicity, porosity surface area and reducibility are manipulated in a complicated

trade-off process in order to tackle certain problems such as reduced catalyst activity or coke formation as shown in **Figure 1**[30].

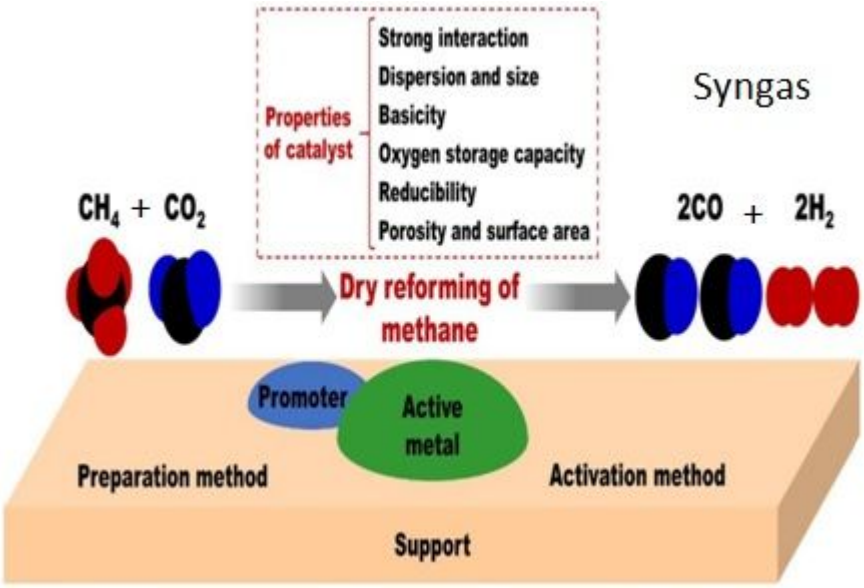

Figure 1 Summary of catalyst properties for DRM catalyst design modified from[30].

1.3 Carbon deposition mechanism and coke management

There is no doubt that carbon deposition on Ni-based catalyst used in DRM limits its application and effectiveness. However the problem of coke deposition cannot be solved away from other challenges. In fact, designing a catalyst for DRM is a complicated trade-off process that need tackle certain problems such as carbon deposition-as in **Figure 2**- and reasonable activity[31].

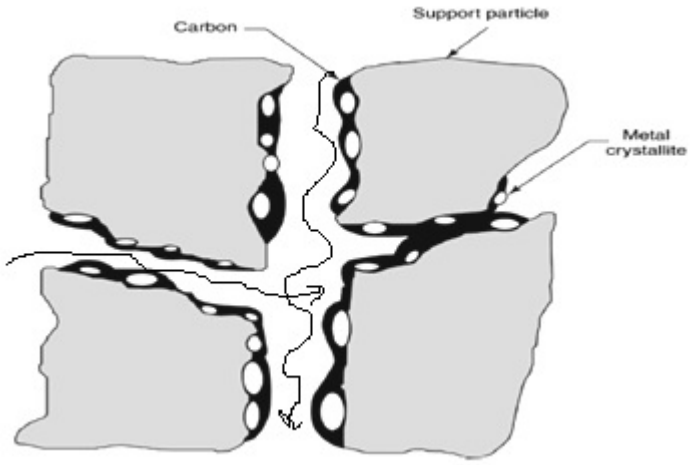

Figure 2 Pore plugging in a supported metal catalyst owing to carbon adapted from[18].

Table 1 Different carbon species formed on the catalyst modified from[18]

Carbon Structure	Designation	Temperature range (degC)
Adsorbed, atomic carbon (surface carbide)	$C_{\alpha(alpha)}$	200-400
Polymers, amorphous films	$C_{ß(Beta)}$	250-500
Ni carbide (bulk)	$C_{Y(gamma)}$	150-250
Vermicular filaments or whiskers	$C_{v(filamentous)}$	300-1000
Graphite (crystalline) platelet films	$C_{c(crystallline)}$	500-550

DRM is usually associated with competitive reactions such as Boudouard reaction, Reverse water–gas shift (RWG), methane cracking and methanation. Among these reactions, Boudouard reaction and methane cracking are responsible directly for carbon formation which causes rapid catalyst deactivation as in **Table 1** and **Scheme 1**.

Boudouard reaction :

$$2CO \rightarrow Cads + CO_2 \qquad \Delta H^{\circ} = -172 \text{ kJ mol-1} \qquad (2)$$

Reverse water–gas shift:

$$CO_2+H_2 \rightarrow CO+H_2O \qquad \Delta H^{\circ} = 41 \text{ kJ mol-1} \qquad (3)$$

Methane cracking:

$$CO_2+H_2 \rightarrow CO+H_2O \qquad \Delta H^{\circ} = 41 \text{ kJ mol-1} \qquad (4)$$

Methanation:

$$CO_2+4H_2 \rightarrow CH4+2H_2O \qquad \Delta H^{\circ} = -165 \text{ kJ mol-1} \qquad (5)$$

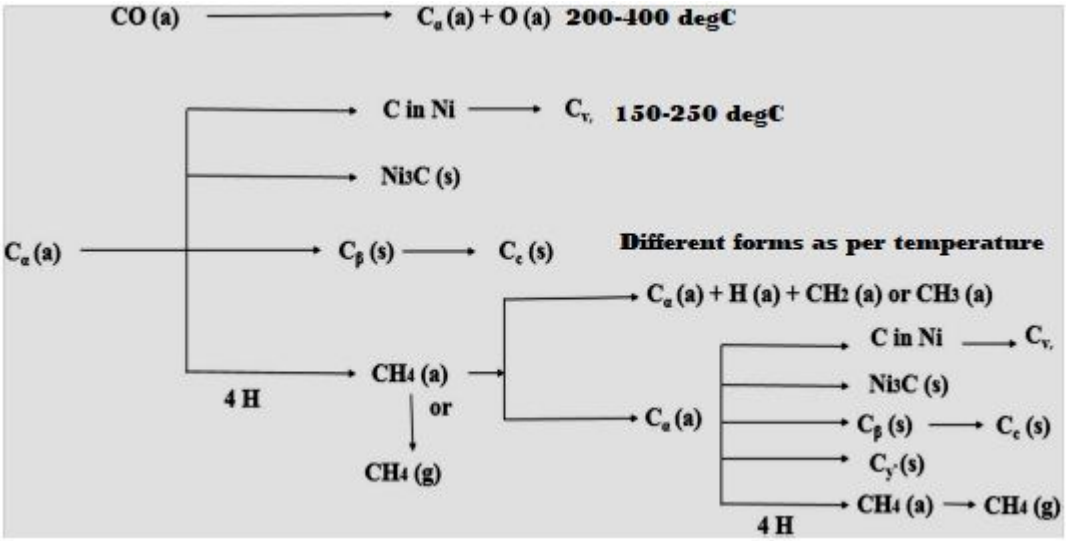

Scheme 1 Mechanism of carbon formation at the catalyst surface adapted from [18].

Temperature control plays crucial to avoid these side reactions as well as manage coke formation. While methanation are favored at lower temperature (300°C), Boudouard reaction generate less reactive species at temperatures (500-700°C) which deposits on metal.

Increasing the temperature to above 800°C inhibits the highly exothermic Boudouard reaction and more reactive carbon species are formed mainly due to methane cracking which can be easily oxidized by CO_2. In other words, coke formation is minimized as carbon removal by CO_2 is equivalent or faster than carbon formation. However, these high temperature operation demands more energy, which represents an economic challenge for DRM industrial applicability while produce more CO_2 if the energy source is fossil fuel. Recently, Wang et al[28] suggested utilizing promoters such as

Ce and Zr in optimum process parameters can lower this temperature with enhancement of the ability of carbon deposition elimination and carbon deposition resistance[28].

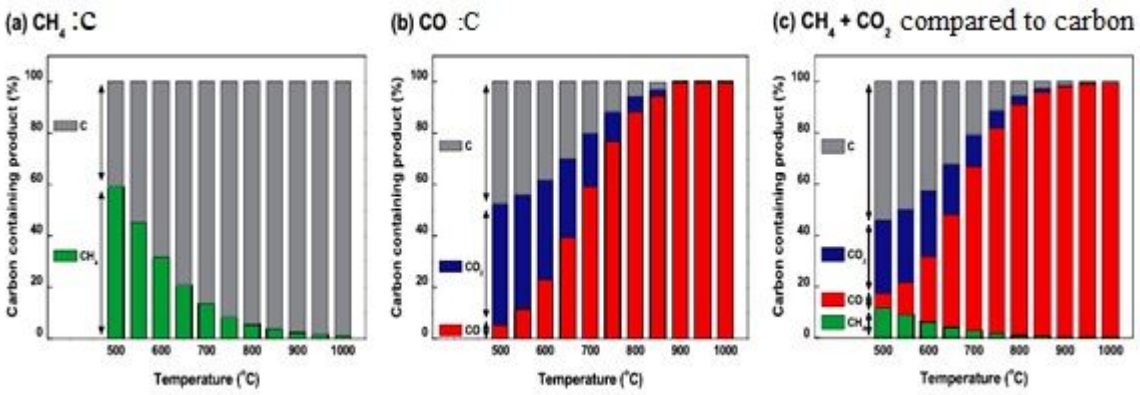

Figure 3.Carbon containing product for the catalytic reactions: (a) CH_4 decomposition (CH_4=100%), (b) Boudouard reaction (CO=100%), (c) Dry reforming of methane (CH_4=50% and CO_2=50%) modified from[30].

To illustrate the kinetic and thermodynamics of DRM, let C_X (X= A, B, or R) is the component concentration and k0 is the frequency factor, as determined by the Arrhenius law, equilibrium constant K, absolute temperature T, activation energy E_a, while k_0 is the pre-exponential factor, and R is the universal gas constant.

From Arrhenius Equation**:**

$$k = k_0 \exp(-E_a/RT) \quad (6)$$

Forward reaction rate constant:

$$r_f = k_f(C_A, C_B),\ k_f = k_{0f} \exp(-E_a/RT) \quad (7)$$

Reverse reaction rate constant:

$$r_r = k_r(C_R),\ k_r = k_{0r}\exp(-E_a/RT) \quad (8)$$

So one can conclude that the equilibrium constant $K=k_f/k_r$; which determine the DRM extent. As implied from above **Figure 3** and **Figure 4**, methane decomposition occurs at temperatures above 557°C and the Boudouard reaction at temperatures below 700°C.Thus, maximum carbon deposition is reported in the temperature range 557–700°C, as shown in the equilibrium data for the DRM reaction[32].

Zhu et al[36] conducted a comprehensive DFT study for DRM over Ni (111) catalyst to investigate the reaction mechanism . They observed that the dominant pathway for DRM includes CO_2 direct decomposition to form atomic O as well as methane dissociation to generate CH and C, followed by the CH and C oxidation by atomic oxygen and finally decomposition of CHO to produce CO. However, they stressed that the OH oxidant effect cannot be ignored [33].Tomishige et al[38] tried to investigate carbon deposition source and conclude that carbon formation fromCH_4dissociation is more than that formed from CO disproportionation and that may be attributed to the fact that CH_4 dissociation promoted Ni aggregation than CO[34]. In two separate publications, Trimm et al[35] investigate the role of Ni_3C in DRM and concluded that formation of nickel carbide is crucial step in coke formation over Ni- based catalysts[36].

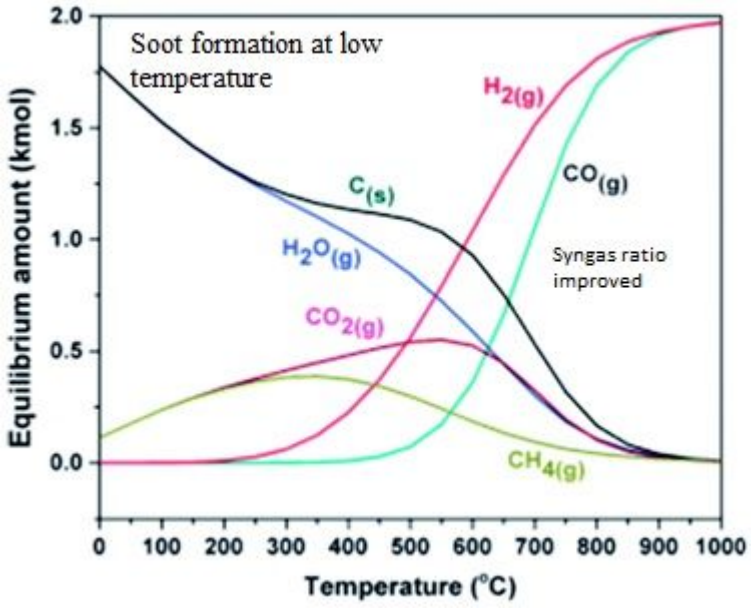

Figure 4.Equilibrium data for DRM process adapted from[18].

The same conclusions have been confirmed by DFT studies. Ziyun et al[37] focused on carbon deposition mechanism on Ni different surfaces as shown **Figure 5.** The study showed that carbon deposition is sensitive to Ni metal surface structure and emphasis on the main role of Ni_3C on rapid carbon deposition that leads to rapid catalyst deactivation. Moreover, carbon diffusion and segregation on the Ni surface is related to surface structure. Surface modification is with no doubt- a key factor to inhibit coke formation during DRM. It has been found that carbon diffuse more in Ni surfaces in the following order: 110>100>111[37].

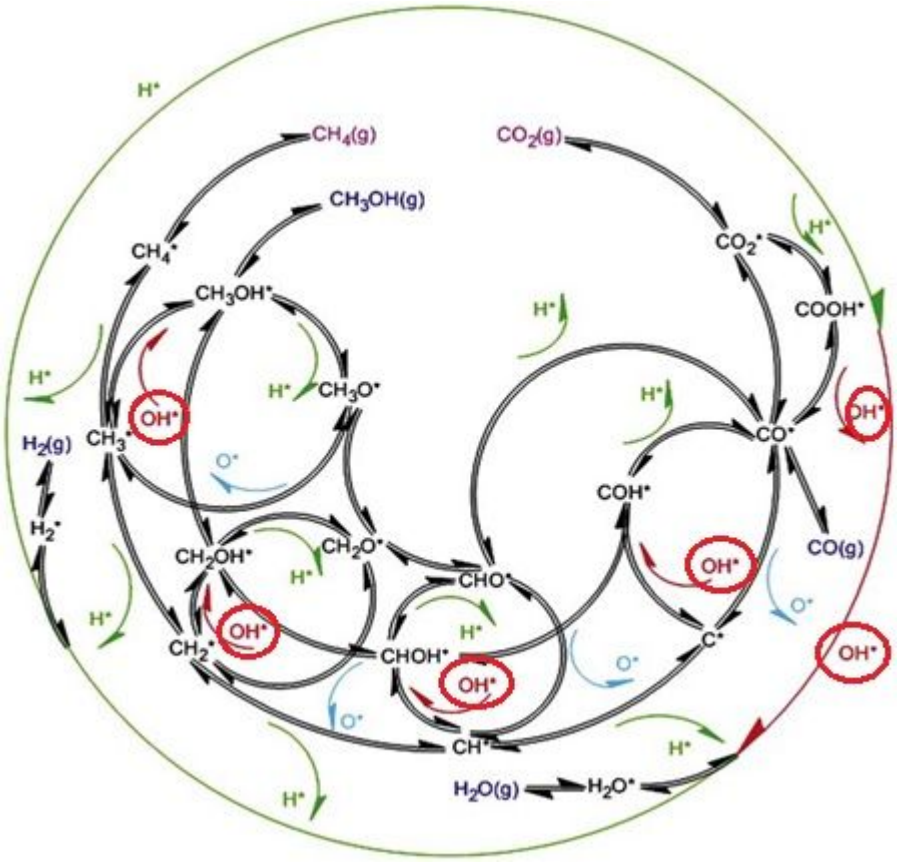

Figure 5 Proposed mechanism for dry reforming of methane on Ni catalyst modified from[33] to show OH species role.

Experimentally, this claim has been confirmed by plasma techniques which ensure that Ni (111) lattice structure is well-defined with proper Ni dispersion, reduce particle size and ensure the strong metal-support interaction (SMSI). The result of this well-define structure was high catalytic activity and excellent resistance to formations of filamentous carbon and encapsulating carbon[38,39]. **Figure 6** shows schematically the phase transformation and coke formation Ni(111) and Ni(211) stand for the clean nickel metal flat and stepped surfaces respectively, and $Ni_3C(001)$ and $Ni_3C(111)$ are the flat

and stepped nickel carbide[37]. Flat surfaces are marked in blue, while stepped surfaces are in red. Toxic coke is the more stable and high toxicity carbon atom which will result in the deactivation of the nickel catalyst. The corresponding overall reaction rates are marked below the different structures. The arrow with **X** means this step is not likely to occur, while arrow without X means this step could happen[37].

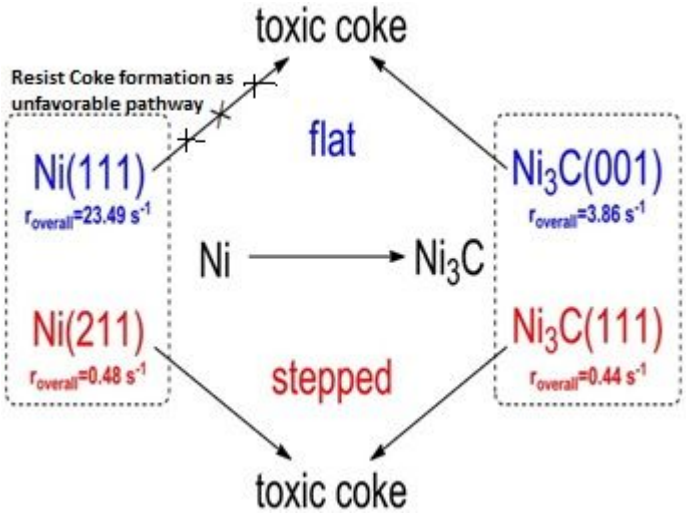

Figure 6 Deactivation scheme to show schematically the phase transformation and coke formation adapted from [37].

Particle size is another main factor that can control carbon deposition. Under the DRM high temperature conditions the Ni particle easily agglomerate due to thermal sintering[40,41]. Kim et al[46] showed that 7 nm is the lowest diameter for Ni nanoparticles (NPs) to enable filamentous carbon formation[42]. Nicolas et al[31] highlighted the need for a fine catalyst particle size, ideally below 5 nm, to avoid excessive carbon deposition[31].

Several strategies can be utilized to control the nickel particle size and hence reduce coke formation: (1) Enhance the dispersion of Ni during preparation[43,44], (2) Improve Ni capacity for anti-sintering by SMSI [45,46] and (3) Use a core-shell and mesoporous support to improve the confinement effects as in **Figure 7**[47,48].

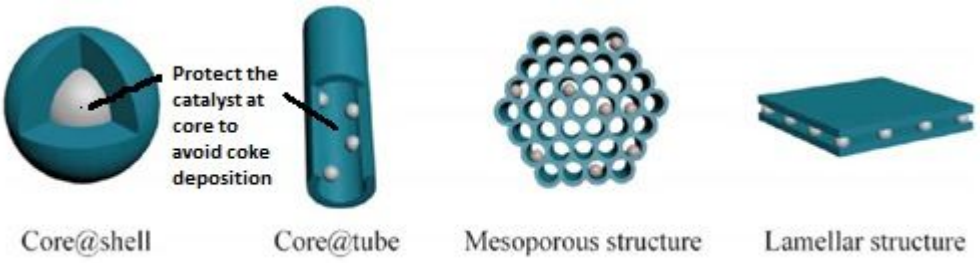

Figure 7 Categories of the Catalysts with Encapsulated Structures adapted from[49].

1.4 Bimetallic Ni-based catalysts for DRM

Recently Ni bimetallic catalysts have received a lot of attention and research due to its practicality. Doping other metals in Ni-Ni network results in synergistic effect due the change of metal surface properties which, in turn, improves the catalytic activity and improve carbon resistance[30,50,] For DRM reaction, Ni can be coupled with either noble or transition metals. The former option has recently received due to its availability and cheap price, which enables long term operation without frequent shutdowns for catalyst change or regeneration. **Figure 8** summarizes different bimetallic alloys and their characteristic properties.

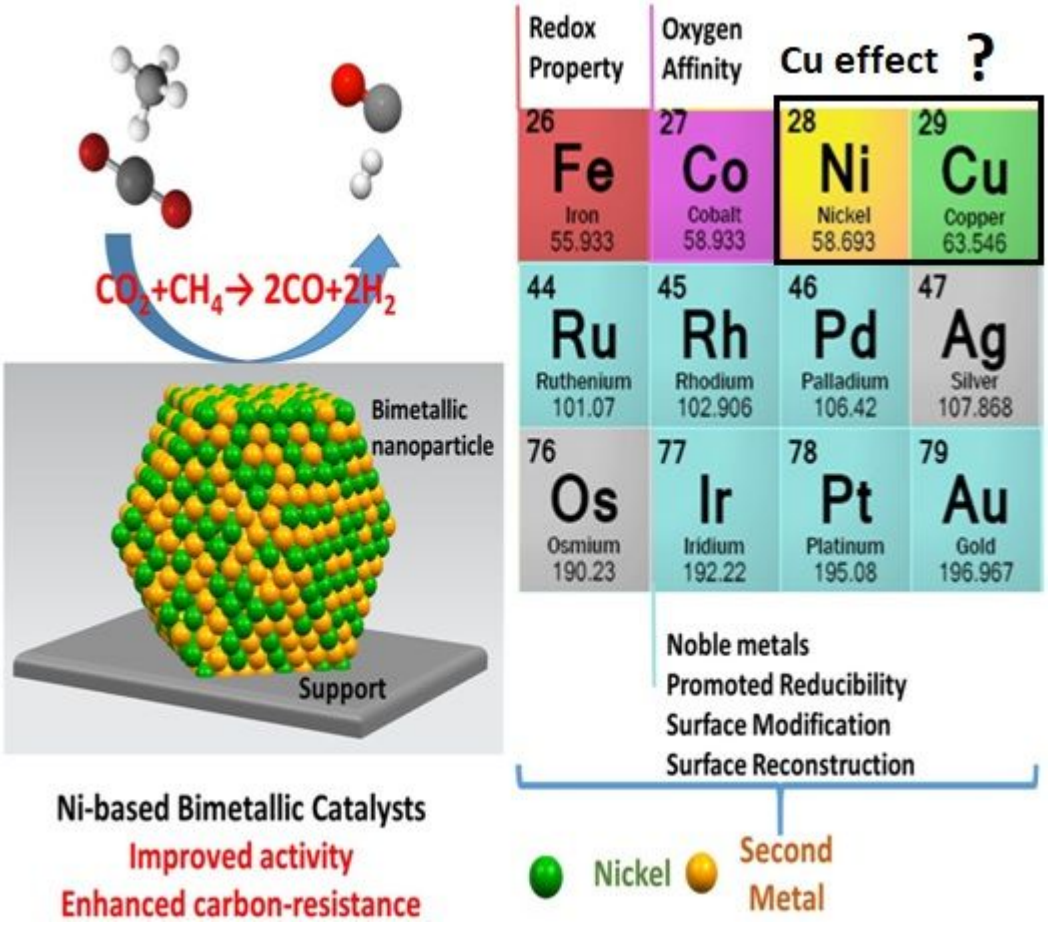

Figure 8 Summary of characteristic properties of different Ni-based bimetallic catalyst. Cu requires further study to interpret its properties on molecular level modified from [26].

1.4.1 Bimetallic Ni-noble metal catalysts for DRM

Noble metals such as Ir , Ru and Pt are used frequently for DRM because they exhibit high catalyst activity and less coke formation[25,51,52].However, their application is limited due to less availability and high cost. Foppa et al[53]used DFT calculations to explain coke resistance of noble metals by comparing DRM and competitive reactions free energy span. Their study[57] showed that Boudouard reaction results in less reactive

carbon form on Ni that cannot be easily removed. On the other hand, more reactive coke - which can be easily oxidized –is formed on Pd and Pt from methane cracking reaction [53].Catalyst activity and carbon resistance depends for a major extent on its reducibility. On a catalyst with suitable reducibility, the produced syngas can reduce the oxidized and deactivated catalyst. Moreover, the catalyst fluidization inhibited the carbon deposition[54].

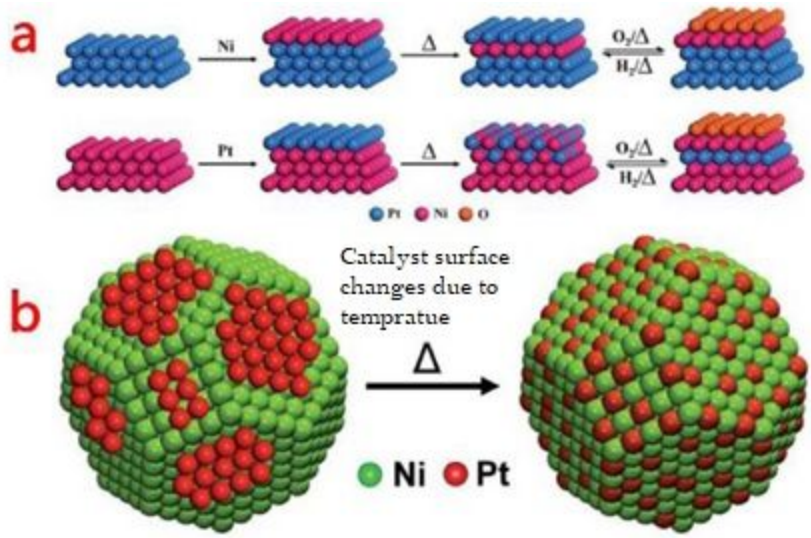

Scheme 2 a) Surface restructuring of Ni-Pt bimetallic systems induced by temperature and adsorbates; **b)** Evolution of the surface structure of Ni/Pt bimetallic nanoparticles upon thermal treatment adapted from[55].

Hydrogen spillover effects occurs when hydrogen molecules dissociate on noble metal and diffuses to non-noble metal species increasing its reducibility[56]. Decorating the Ni surface with small amounts of noble metals will modify its surface and even lead to surface re-construction to become similar to the core-shell pattern-as in **Scheme a/b**- with the Ni-rich core is protect from carbon deposition and enhanced activity [55]**.**

1.4.2 Bimetallic Ni-transition metal catalysts for DRM

Transition metals such as Cu, Fe, Co showed intrinsic characteristics to improve both catalyst activity and resistance to coke formation [57].

Co was used as both mono and bimetallic catalyst for DRM [58,59]. Cobalt-based catalyst exhibits high CH_4 conversion for continuous 250 h TOS (Time-On-Stream) with reduced coke formation [60]. It is widely believed that a high metal dispersion or small ensemble size can be enhanced by reducing the Ni–Co content. High metal dispersion is responsible for the Ni–Co outstanding stability, SMSI and coke resistance[60,61]. The enhancement of catalytic activity and stability is thought to be due to its high oxophilicity. While Co is oxidized to Co-O via carbon dioxide, the carbon species from CH_4 dissociation reduce it again to Co^0 resulting in dynamic redox system which maintain catalyst stability.

Ni-Fe catalysts have been also investigated and showed improved coke resistance due to Ni-Fe alloying and re-alloying process. The presence and migration of FeO at the surface allowed its reaction with deposited carbon. This phenomenon explained the increased stability via Fe^{2+}/Fe^0 redox cycle as in **Scheme 3**[62,63] **.** Recently, Xu et al[64] conducted DFT study on DRM over Ni_2Fe of Ni(111) and concluded that the surface C reacts with lattice oxygen of FeO to produce CO via Mars-van Krevelen (MvK) mechanism with a low energy barrier of 0.16 eV as in **Figure 9**, which agrees with the experimental results from Stavros et al [63,64,65]**.**

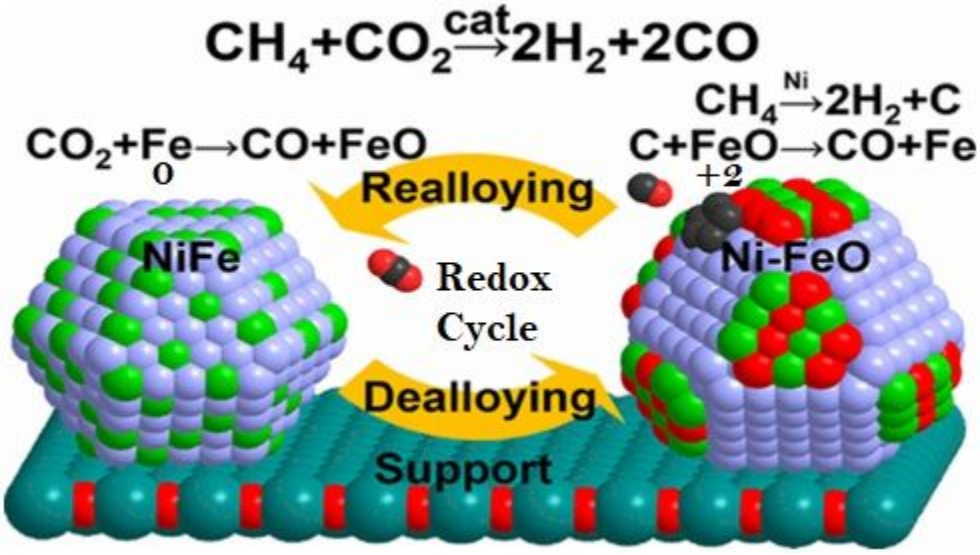

Scheme 3 Dealloying and realloying behavior of an Fe-Ni alloyed particle in DRM modified from [66].

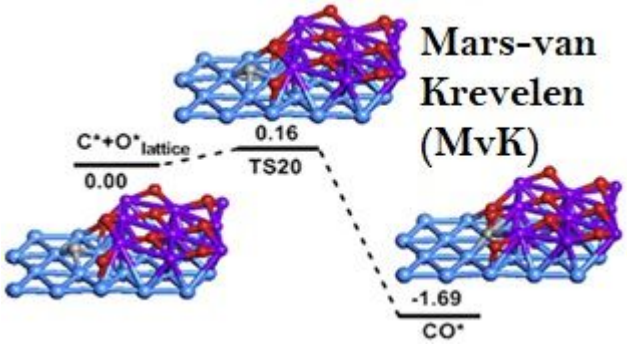

Figure 9 Energy profile of C oxidation by lattice oxygen in FeO/Ni (1 1 1) (in unit of eV). The gray and red balls denote the C and O atoms, respectively adapted from [67].

1.5 Ni-Cu bimetallic catalysts

The Ni-Cu bimetallic catalyst on different supports such as SiO_2 and Al_2O_3 and others has been studied. It has been proven that the incorporation of Cu into Ni-Ni

surface has been proven to enhance stability, promote activity and improve coke resistance in dry reforming. For example, Pendem et al[68] studies the Cu–Ni interfacial interaction and chemical state of the active catalytic phase. By characterization of the fresh and used catalyst, they showed that the Cu- Ni particles intrinsic catalyst synergy may be responsible for the bimetallic catalyst high stability and reactivity, even with good recyclability after ten successive cycles without considerable loss in the activity.

Yet, there is no clear interpretation the role of Cu especially at the molecular level in terms of enhanced carbon resistance to date[26,69, 70].

Cu can act as active phase promoter in CH_4/CO_2 reforming. As per Massimiliano et al[72], the partial substitution of Ni by Cu interrupts the Ni-Ni network and reduces coke formation[69]. While Ni and Fe catalysts have a comparably high catalytic activity and suffer from performance degradation caused by coking, Cu catalyst is less active compared to both catalysts but more resistant to coking.[71] .

Vizcaíno et al[72] proved that Nickel is the phase mainly responsible of hydrogen production by ethanol steam reforming over Cu–Ni supported catalysts, while the copper presence reduces the CO formation and coke deposition[72].Kim et al[73] exposed Ceramic-metal (cermet) composites having alloy compositions of 0, 10, 20, 50 and 100% Ni were exposed to dry reforming of methane at 1073 K for 1.5 h. The experiments demonstrate that coke formation is greatly halted on the Cu-Ni surfaces compared to Ni catalyst. More interestingly, they also noted that carbon formation on the alloys reduced with the increased reduction temperatures[74]. Misture et al[77] showed that oxide-supported metal catalysts has high activity for dry reforming of methane with turnover frequencies as

large as 3.9 at 850 °C. The $Ni^0.375Cu^0.375Mg^0.25Al_2O_4$ catalyst shows stable methane conversion out to 12 h on stream without performance-degrading coking[75].The same outcome was confirmed by Reshetenko et al[76] , Lopez et al[77] and Miriam et al[78].Moreover,Sharifi et al concluded that Cu addition improved feed conversion, products yield and better syngas ratio when he used Cu-promoted Ni/Al_2O_3-ZrO_2 catalyst[79].Similar result was indicated by Bonura et al who concluded that copper addition promotes the kinetics of nickel reduction[80].

In attempt to explain the effect of Cu, Nader et al reformed CH_4/CO_2 over synthesized 2 Ni–Cu/Al_2O_3 nanocatalysts that were prepared separately via impregnation method and treated using non-thermal plasma methods separately. The authors indicate that while stability of the nanocatalyst was attributed to size of NiO crystals, its activity strongly dependents on the morphology and the synergism effect between nickel and copper particles[81]. This synergism effect itself is related to the Cu loading up. Wu et al concluded that a Cu/Ni of 1:3 loading showed higher activity whereas higher Cu content significantly reduces the activation of methane. This can be explained by possibly due to that the competitive adsorption of CH_4 and slow dissociation kinetics on copper atoms. Surface enrichment of copper due to low surface energy compared with Ni may also decrease the number of active Ni sites on the surface and affect activity for high copper ratios [82] .

The above experimental conclusions are in agreement with DFT calculations. Wang et al investigate the effect of doping coinage metals in Ni-Ni network for DRM. The authors focused on the successive dehydrogenation of CH_4, as well as the diffusion

of CH (one of the important carbon-containing intermediate along with CO), on the doped Ni (111) surfaces. He concluded that the adsorption energies of CH*x* (*x*=0-3) are reduced on alloy surface compared to the corresponding adsorption energies on Ni (111) surface. In particular, the Cu-Ni surface makes the CH intermediate product is much more difficult and thus prevents the CH species reactions[60]. Liu et al conducted DFT study to investigate the dissociation of CH_4 on NiCu (111) surface. The results showed that Cu-rich surface shows better coke resistance [83]. The same group studied the dissociations of carbon deposition on (111) catalyst surfaces of both elementary metals (Fe, Co, Ni and Cu) and bimetals (NiFe, NiCo and NiCu). Based on their DFT calculation, they showed that carbon deposition is expected to be least likely to occur on segregated NiCu surface compared to Ni (111) surface[84]. These results agree with An et al[86] who concluded that the activation energy barrier (E_{act}) for CH→C+H on NiCu (1 1 1) is found to be 1.8 times larger than that on Ni(111), while E_{act} for $CH_4 \rightarrow CH_3+H$ is 1.3 times larger [85]. Similar conclusion has been confirmed by Wei et al[86] who studied the methane dehydrogenation on a bimetallic Cu/Ni (111) surface. To conclude, the Cu-Ni surface reduces coke formation by elevating the CH energy barriers. However, the stability of CuNi alloy cannot be fully explained by the ensemble effect of Cu on Ni metal that may inhibit the carbon formation rate on Ni catalyst. More comprehensively, the incorporation of Cu into Ni affects the oxidation pathway of the deposited carbon, and this factor would be more important in the stability control of CuNi alloy[87,88].

Most reports in literature recognize the role of Oxygen (O) species in carbon elimination, Zhang et al[70] highlighted that not only O species but also OH species has

stronger role in carbon elimination in case of Ni (111) and CuNi(111) surface. In their attempt to explain carbon elimination on Ni based surfaces, they have used DFT calculations to systematically investigate the mechanism of surface carbon elimination by O and OH on both the alloy FeNi(111) and CuNi(111) surfaces [70]. Their finding showed a linear relationship between the average adsorption energy of C+O or C+OH species and the activation barrier of C+O or C+OH reactions for carbon formation[70]. Thus, they explained that the ability of carbon elimination on the metal surface increases with the decreasing of adsorption ability for C+O and C+OH species on the corresponding metal surface[70]. In other words, as CuNi(111) surface promotes carbon elimination and inhibit carbon, carbon elimination is accelerated resulting efficient periodic cycle of carbon formation and elimination which may be responsible for the stability of CuNi bimetallic catalysts[70]. So, overall the addition of Cu to Ni catalyst both promotes DRM activity and enhances coke resistance as shown in **Figure 10**[26].

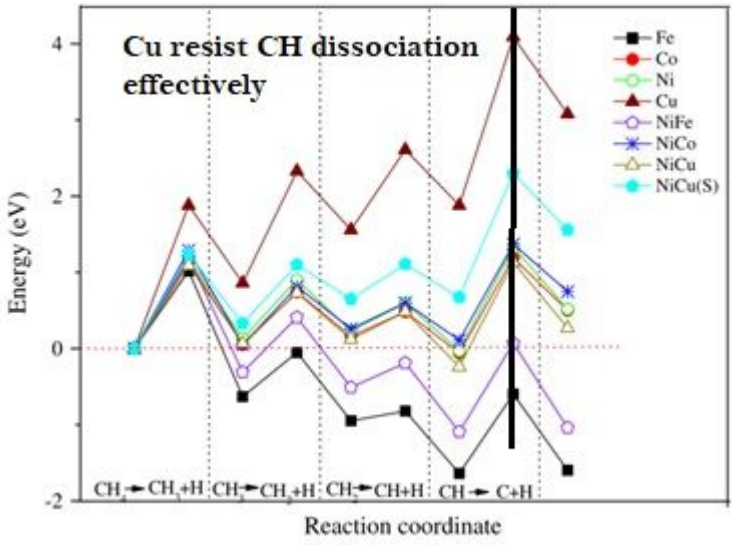

Figure 10 The energy profiles for the dissociation of CH_4 on elementary metals (Fe, Co, Ni and Cu) and bimetals (NiFe, NiCo and NiCu) surfaces modified from[84].

2 RESEARCH PROBLEM AND OBJECTIVES

2.1 Research problem

There is no doubt that climate change is a global problem. GHG emissions are main contributor to climate change. Increasing population and growing industrial activity are main sources of GHGs emissions[89].The world population boom in the second half of 20th century has reached its peak levels with the highest growth rates reported at 2.06% between 1965 and 1970[90].This increase in population has been met with more demand for energy. Although efforts toward making the use of renewable and clean energy more sustainable are continuing[91,92], the fossil fuels such as oil, coal and natural gas are still playing a major role in the energy mix of most countries worldwide.

Syngas production from CO_2 is well-know technology which can results in valuable via Fischer–Tropsch syynthesis[19]. In that context, the dry reforming of methane (DRM) reaction is attractive attention due to its advantages over steam reforming (SRM). DRM require no CO_2 separation from flue gases and lower H_2/CO ratio around unity compared to SRM [23,93].

Different catalyst have been explored for DRM, among them Nickel and Ni-based catalysts been showed reasonable activity that can be compared to noble metals which are less available and expensive[25,52]. However, as no oxygen is directly involved in dry reforming, the carbon deposition on the reaction catalyst represents a major drawback that hinders further industrial application[94].Several nickel-transition metals bimetallic catalyst showed their potential for coke resistance and improved activity. Co and Fe synergistic characteristics are due to their oxophilicity and redox system respectively[50,70].

However, Cu behavior of coke resistance and activity enhancement is still not well defined at the time of this study. DFT study for DRM over copper modified Ni (111) catalyst is performed to explore the reaction mechanism, barrier energies and coke resistance behavior.

2.2 Research objectives

1. Study the adsorption of all different species involved in DRM over Ni_2Cu layer to identify the most stable configurations.
2. Investigate the dominant reaction mechanism of the dry methane reforming of methane over Ni_2Cu bimetallic catalytic system.
3. Explore coke removal oxidation by both atomic O and hydroxyl group (OH).
4. Compare C elimination by Cu surface enrichment to similar Ni_2Fe and mono metallic Ni (111) catalysts reported in literature.
5. Evaluate the Cu surface enrichment and Temperature effect on both coke deposition and catalyst activity.

3 METHODOLOGY

3.1 Methods and calculation parameters

Density functional theory (DFT) is a phenomenally successful approach to finding solutions to the fundamental equation that describes the quantum behavior of atoms and molecules that have been described by the Schrödinger equation. There are two important definitions related to Schrödinger equation solution and DFT: the wave function and the ground state. The definition of wave function is quantum physics state that it is a mathematical description of the quantum state of a system. The ground state of a quantum system is its lowest-energy state; the energy of the ground state is known as the zero-point energy of the system. On the other hand, an excited state is any state with energy greater than the ground state.

Schrödinger equation in its famous simple form is:

$$\hat{H}\,\Psi = E\Psi \tag{9}$$

In this equation the $\hat{H}$ is Hamiltonian operator and Ψ is a set of solutions of the Hamiltonian. For each of these solutions Ψ has an associated eigenvalue, E_n, which is a real number that satisfies the eigenvalue equation.

Born-Oppenheimer Approximation stated that since the electrons are small and fast compared to nuclei then the dynamics of nuclei and electron can be separated or decouple into two wave functions as follows:

$$\Psi(\{r_i\},\{R_I\}) \rightarrow \Psi_N(\{r_i\},\{R_I\})^* \Psi_e(\{r_i\},\{R_I\}) \tag{10}$$

For a fixed set of atomic positions, the focus of the calculation is to solve the ground state of the electrons.Where $\mathbf{r_i}$ is the spatial coordinate of each i electron and R_I is the spatial coordinate of each I nucleus.

Based on the above, the Schrödinger equation can be expressed as follows:

$$\hat{H}\,\Psi\,(r_1, r_2, r_3 \ldots r_N) = E\Psi\,(r_1, r_2, r_3 \ldots r_N) \quad (11)$$

Where Ψ is the electronic wave function, which is a function of each of the spatial coordinate r of each of the N electrons. Solving Schrödinger equation will enable the determination of the ground state of a collection of atoms **Figure 11**gives a closer look at the Hamiltonian component of Schrödinger equation.

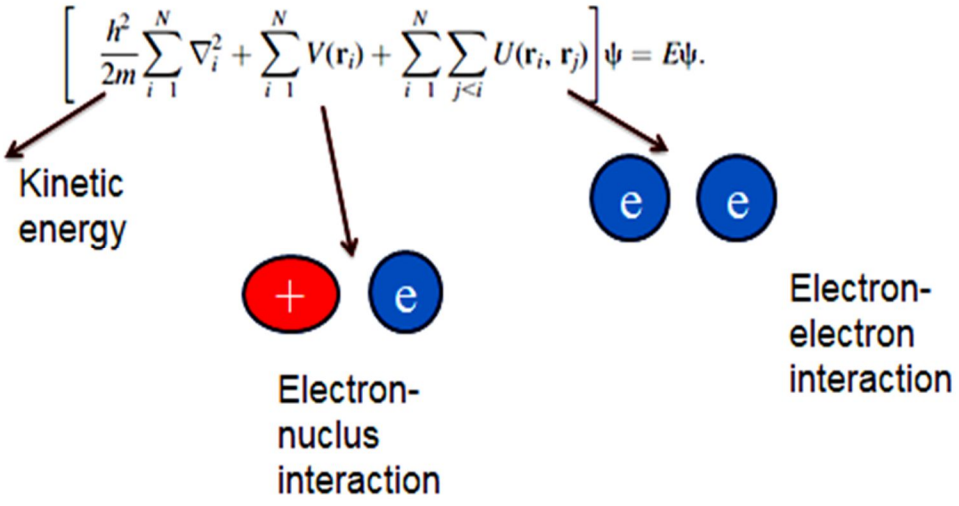

Figure 11 Electronic Hamiltonian components modified from [95]

Still, to solve Schrödinger equation for simple molecule is computational challenge as it has many-electrons problem. To illustrate this problem, consider the water molecule which possesses 10 electrons only, the Schrödinger equation will become a 30-dimensional problem as we consider 3 spatial coordinates per electron position. Similarly, we can say carbon dioxide Schrödinger equation, which will be 66-dimensional problem and so on.

The strength of the Density Functional Theory (DFT) comes from its capability to utilize the electron density **n(r)** which is a true observable – a physical quantity that can be measured by methods such as X-ray diffraction-that contains all information in wave function. This closely related quantity is the density of electrons at a particular position in the space since it can be written in terms of the individual electron wave functions as follows:

$$\mathbf{n(r)} = 2 \sum_i \Psi_i^*(r)\, \Psi_i(r) \qquad (12)$$

The summation goes over all the individual electron wave functions that are occupied by electrons, so the term inside the summation is the probability that an electron in individual wave function Ψ_i **(r)** is located at position r. The factor of 2 appears due to Pauli Exclusion Principle, which states that each individual electron wave function can be occupied by two separate electrons provided they have different spins. The n(r) is function of 3 coordinates instead of 3N coordinates in case of Schrödinger equation, which converts the many-electrons problem to many-one electron problem.

The density functional theory is based on two fundamental mathematical theorems proved by Kohn and Hohenberg and the derivation of a set of equations by Kohn and Sham in the mid-1960s[96,97]. The first theorem, proved by Hohenberg and Kohn (HK), is: The ground-state energy from Schrödinger's equation is a unique functional of the electron density. This is very important as it support the elaborate the concept discussed above. In fact, it is possible to solve the Schrödinger equation –or in other meaning find the ground state of atoms- by finding a function of three spatial variables, the electron density, rather than a function of 3N variables, the wave function. In addition, the second Hohenberg–Kohn theorem defines another important concept of the functional: The electron density that minimizes the energy of the overall functional is the true electron density corresponding to the full solution of the Schrödinger equation[95]

The self-consistent iterative nature of Khon-Sham theory is broken into the following steps:

1. Define an initial, trial electron density, n(r).
2. Solve the Kohn–Sham equations defined using the trial electron density to find the single-particle wave functions, Ψi (r).
3. Calculate the electron density defined by the Kohn–Sham single particle wave functions from step 2,

$$n_{KS}(r) = 2\sum \Psi i\,(r)^* \Psi i\,(r) \qquad (13)$$

4. Compare the calculated electron density, $n_{KS}(r)$, with the electron density used in solving the Kohn–Sham equations, n(r). If the two densities are the same, then this is the ground-state electron density, and it can be used to compute the total energy. If the two densities are different, then the trial electron density must be updated in some way. Once this is done, the process begins again from step 2.

In this project, the first-principles calculations performed in this study are based on spin-polarized Density Functional Theory. The Vienna ab initio package (VASP) is used to simulate DFT calculation. The exchange and correlation of the Kohn–Sham theory are treated with the generalized gradient approximation (GGA) with Revised Perdew-Burke-Ernzerhof [98,99].

The energy cutoff of plane wave was set to 400 eV is used in the all present calculations and all geometries are optimized using a force-based conjugate gradient algorithm [100] until the forces acting on each atom are converged better than 0.01 eV/A˚. Spin polarization was taken into consideration in all calculations due to presence of magnetic atoms. The optimized lattice constant for Ni is 3.523 ˚A which is in good agreement with the experimental value of 3.524[67].

Brillouin zone sampling is performed using a Monkhorst–Pack grid [101] and electronic occupancies are determined according to a Methfessel–Paxton scheme [102] with an energy smearing of 0.2 eV. The Ni_2Cu (1 1 1) surface is represented as a four-layer slab with p (3 x 3) supercell and only the bottom layer of the slab is kept constrained. The neighboring slabs are separated by a vacuum region of 12A˚ .The first Brillouin zone of the p (3 x 3) supercell is sampled with a 3 x 3 x 1 k-point grid, which are evidenced to be

sufficient for this cell. The climbing nudged elastic band[103] and then dimer methods [104]are used to locate the transition state, in which the saddle point is optimized using a force-based conjugate gradient method until the maximum force in every degree of freedom is less than 0.01 eV/A˚. In order to obtain accurate forces, the total energy and band structure energy are converged to within 1 x10^{-7} eV/atom during the electronic optimization.

The adsorption energy (E_{ads}) of surface species on Ni_2Cu overplayed Ni (1 1 1) has been calculated using the following equation:

$$E_{ads}=E_{gas\text{-}surface}-(E_{surface}+E_{gas}) \quad (14)$$

where E_{ads} , $E_{gas\text{-}surface}$, $E_{surface}$ and E_{gas} are the adsorption energy, total energy of adsorbed species , total energy of surface and corresponding gas species, total energy of Ni_2Cu overplayed Ni (1 1 1) and the total energies of gas species respectively[37].

As agreed in literature, the more negative adsorption energy indicates that the gas species is more strongly adsorbed on the surface[105,70]. The transition state and minimum energy paths are obtained using the climbing-image nudge elastic band (Climbing-NEB) method and confirmed by single imaginary frequency from vibrational analysis[103,106,107]. All calculations have been performed on RAAD2 supercomputer at Texas A&M University at Qatar. RAAD2 is a Linux based system from the vendor Cray and has a total of 4,128 traditional CPU cores of the Intel Haswell architecture. Each of its 172

compute nodes contains 24 physical CPU cores -- 2 processor sockets with 12 cores per socket -- and 128GB of RAM. The interconnect is comprised of the Cray Aries network, which is employed both for MPI as well as storage traffic. Raad2 runs SLURM as its workload manager, and is paired with a storage system from the vendor DDN that uses the parallel filesystem Lustre, providing 800TB of usable disk capacity accessible from all nodes[108].

4 RESULTS AND DISCUSSION

Ni2Cu over-layered Ni (111) surface properties have been investigated. First, the adsorption and co-adsorption energies have been calculated in **Table 2**. After determining the initial and final state of each elementary reaction of DRM, transition states have been calculated and confirmed by vibrational analysis. Then zero-point energy correction and rate constant have been evaluated .As a result of that, the dominant pathway and rate-limiting step have been confirmed. These steps are explained in **Figure 12**

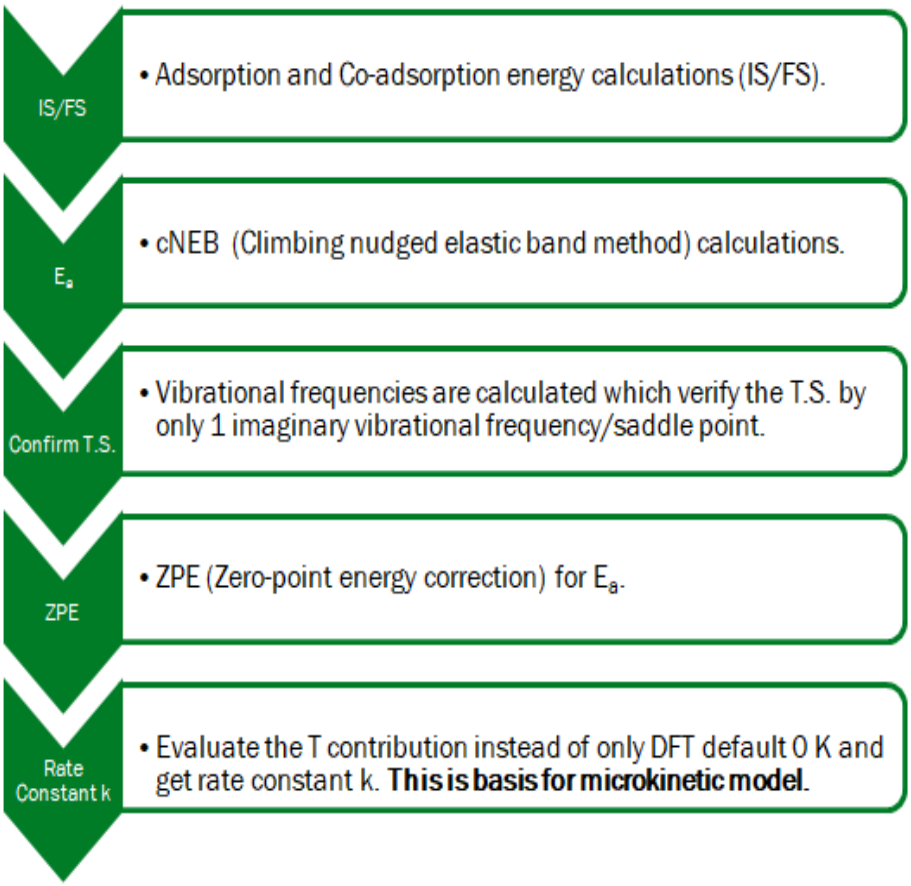

Figure 12 Sequence of DFT calculations shows workflow for DRM over Ni-Cu surface.

	Species	ΔE_{ads}(eV)[a]	Favored adsorption site
1	CH_4	-0.024	N/A
2	CH_3	-2.165	FCC
3	CH_2	-4.997	FCC
4	CH	-5.432	FCC
5	C	-7.044	HCP
6	O	-6.339	FCC
7	OH	-3.275	B^{2Ni}
8	CO	-1.518	B^{2Ni}
9	COH	-4.072	$B2^{Ni}$
10	CHOH	-2.401	B^{2Ni}
11	CO_2	-0.034	N/A
12	H	-3.608	FCC
13	H_2	-0.056	N/A
14	CH_3O	-2.4	B2Ni
15	CH_2O	-0.036	N/A
16	CH_2OH	-1.865	Top^{Ni}
17	CH_3OH	-0.045	N/A
18	CHO	-2.054	Top^{Ni}
19	COH	-4.072	$B2^{Ni}$
20	H_2O	-0.056	N/A
21	COOH	-2.278	Top^{Ni}

[a] Zero-point energy correction are not included

Table 2 Calculated adsorption energies of the species involved in DRM on Ni_2Cu overplayed Ni (111) surface.

As shown in **Figure 13** below, three different sites can be identified: (1) Two top sites (Top^{Ni} and Top^{Cu}) ,two bridge sites (B^{2Ni} and $B^{NiCu)}$ and two hollow sites (HCP and FCC). The optimal structures of all involved species are selected after examining all likely adsorption structures by considering only the most stable configurations on the

$Ni_2Cu(111)$ overlayer used. The values of the corresponding parameters are given in Table 2. All possible reaction paths were considered. However, only the minimum energy path (MEP) of each elementary step was selected. The potential energy profiles of optimized structures of initial states (ISs), transition states (T.Ss) and final states (FSs) are shown. Then, the transition states obtained were confirmed by a single frequency from vibrational analysis. Both T.S and I.S real frequencies have been used for rate constant calculations.

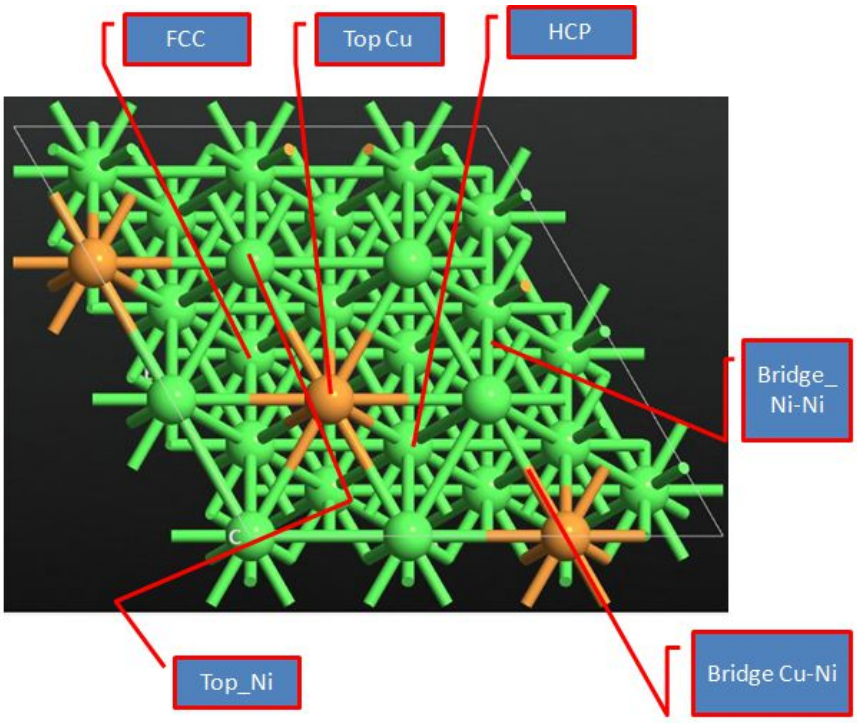

Figure 13 Ni_2Cu overlayer of Ni (111).

4.1 Mechanism of CH_4 dissociation

4.1.1 Adsorption of CH_x species on Ni_2Cu overlayer Ni (111) surface (x=1-4)

DRM turnover rate of DRM is solely limited by C-H bond activation regardless of concentration of reactants[109]. Consequently, it is expected the CH_4 is consumed via dissociative adsorption regardless of CO_2 concentration. Then, the resulting CH***x*** species are either subsequently oxidized by atomic oxygen and OH species to form CH_xO and CH_xOH species respectively or further dehydrogenated.

CH_4 have been found to be physically adsorbed at the HCP site. The adsorption energy is weak with a value around -0.022 eV. On the other hand, CH_3, CH_2 and CH are strongly adsorbed via carbon atom on FCC site with corresponding adsorption energy of -2.17,-4.99, and -5.43 eV, respectively. Similarly, it has been found that H tends to be adsorbed to the FCC site. These results are in good agreement with results of Ni_2Fe overplayed and pure Ni (111) surfaces[33,64,65].

4.1.2 CH_x dissociation (x=1-4)

The successive steps of CH_4 dissociation start with physical adsorption of $CH_{4\,(g)}$ on Ni_2Cu surface to CH_4*. This step showed weak adsorption energy of -0.02 eV.

Then, activation energy of the first step of CH_4 dissociation is calculated to be 1.30 eV as shown in **Figure 14**.

T.S. configuration is showing the detached H atom is located at HCP ,and the remaining CH_3 fragment settle down at 2.08 to achieve maximum C-H-Ni three-center bonding[60,110].After CH_4 is dissociative adsorption on the Ni_2Cu surface, the two

subsequent dehydrogenation steps of CH_3 and CH_2 species are more facile with 0.75 eV and 0.49 eV and endothermicity by 0.33 and exothermicity of 0.066 eV, respectively. So, the generation of $CH_3O(H)$ as well as $CH_2O(H)$ is relatively quiet difficult because the energy barrier of CH_3 and CH_2 dissociation are relatively lower than those for the oxidation (1.37 and 1.6 eV) for CH_3 oxidation, 0.76 and 0.78 eV for the CH_2 oxidation. CH_3OH could be formed from CH_3, CH_3O or CH_2OH intermediates which mainly formed from CH_2 and CH_3 oxidation. Among these intermediates CH_2OH is the most favorable with 1.07 eV energy barrier to overcome.

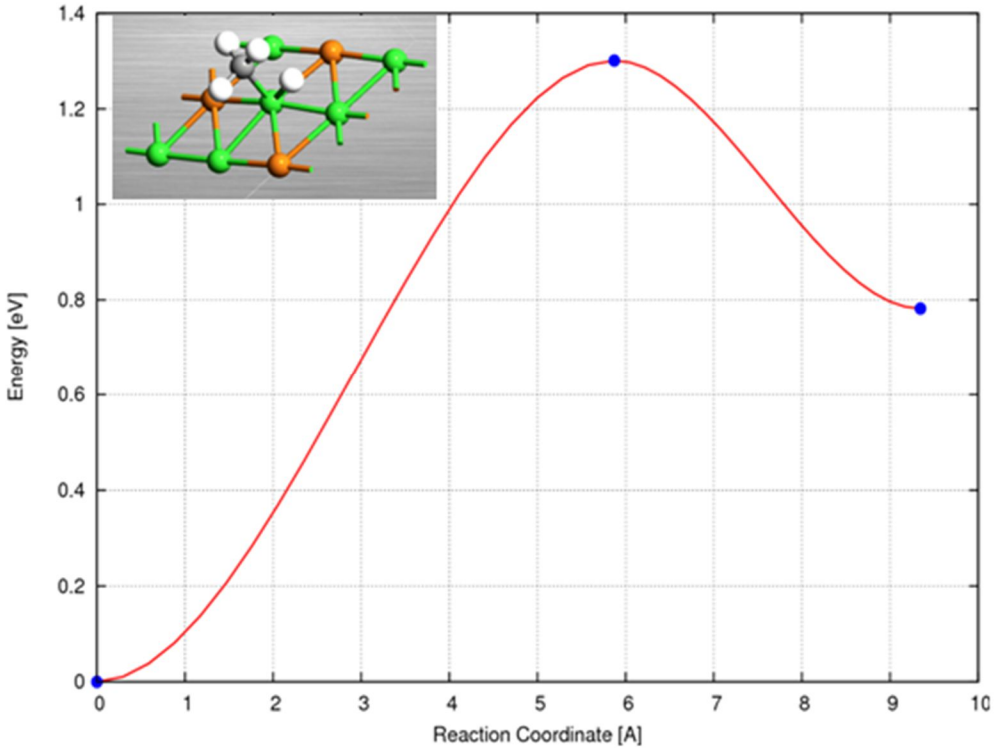

Figure 14 Activation energy profile of CH_4 dehydrogenation. Gray frame is showing T.S. configuration where CH_3 and H are co-adsorbed on Top^{Ni}.

As for CH decomposition, the activation energy barrier increased significantly to 1.41 eV which is higher than those of CH oxidation by OH and O species (1.08 and 1.06 eV) respectively. Based on above results, one can conclude that CH dissociation is the rate-limiting step for CH_4 dissociation process as in **Figure 15**.

In conclusion , the energy barriers for CH_x (x=1-4) bond dissociation increase in order of $CH_2<CH_3<CH_4<CH$, which is in line with CH_4 decomposition on pure Ni(111) and Ni_2Fe systems[64,111].Moreover,CH3 prefers further dehydrogenation than oxidation as in **Figure 16** The comparison Ni_2Cu and those systems clearly indicate that doping Cu into Ni (111) surface has greatly reduced carbon deposition from CH radical dehydrogenation

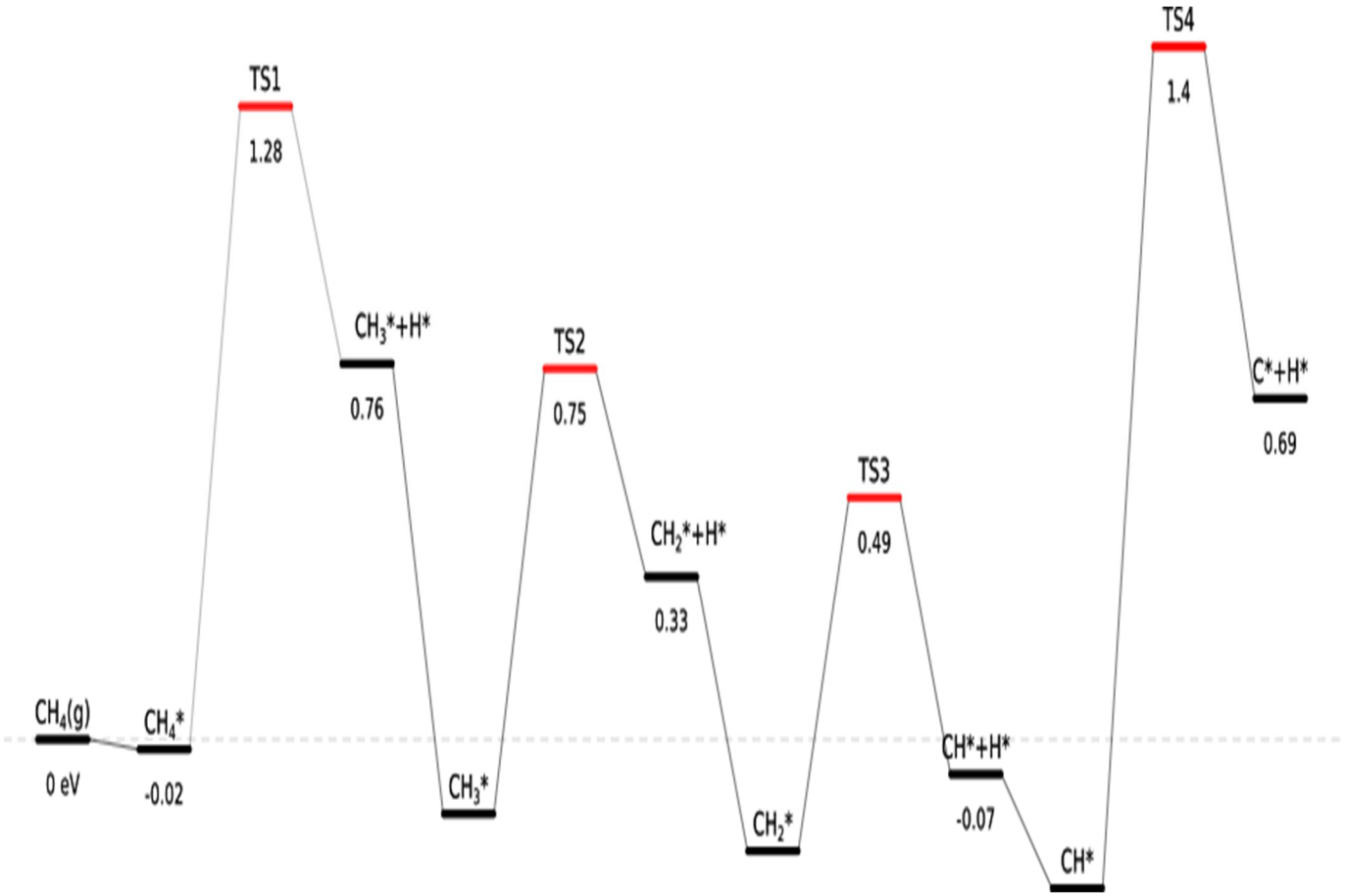

Figure 15 Activation energy profile for CH_4 dissociation steps.

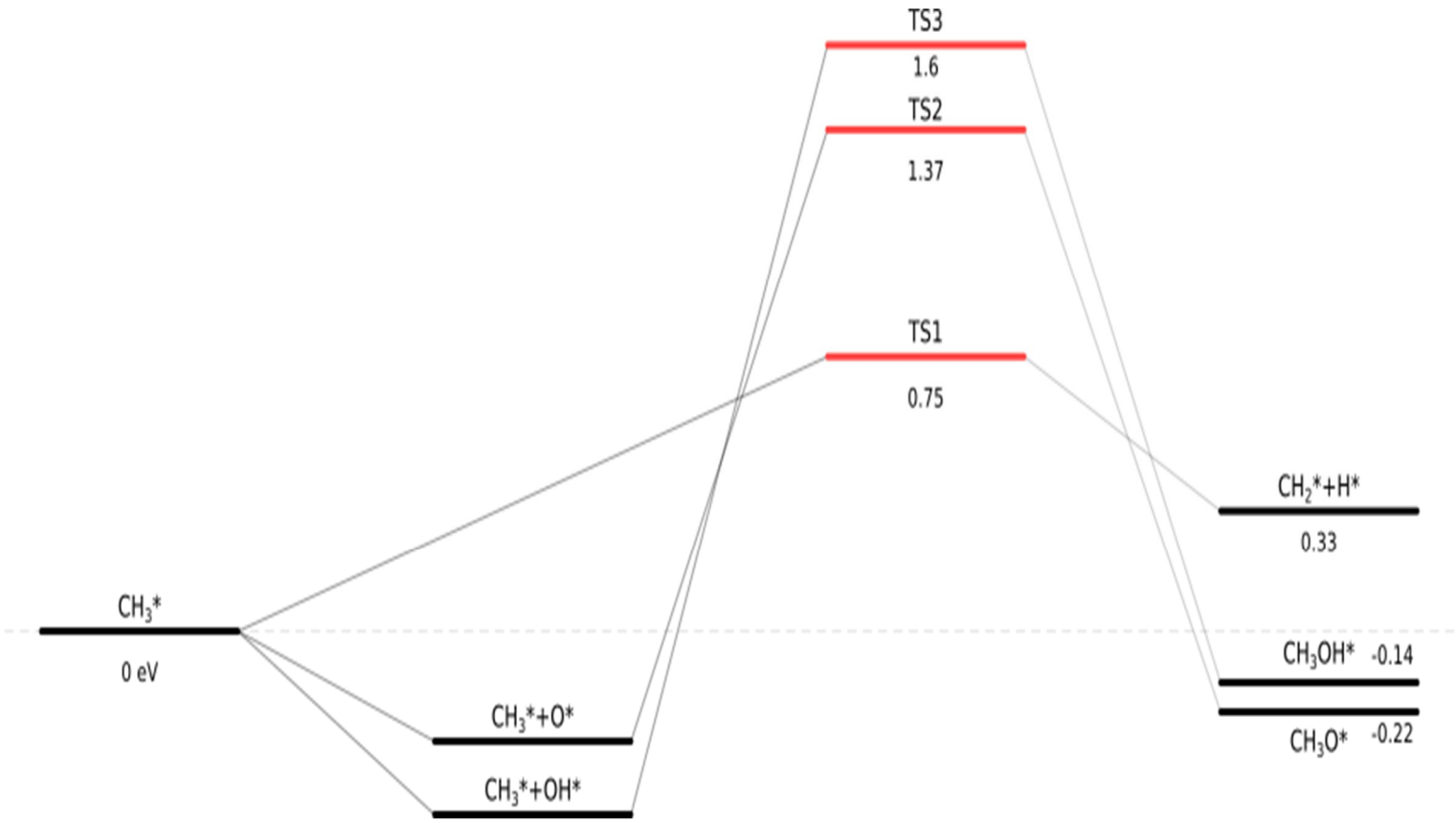

Figure 16 Activation energy profile for different CH_3 possible pathways. It has been found further dehydrogenation is favored over oxidation. Similar pattern has been noticed for CH_2.

4.2 Mechanism for CO_2 decomposition

As it has been expected from experimental work [112,113], CO_2 decomposition have two possible pathways. First, the adsorbed CO_2 dissociates directly to form CO and atomic oxygen. The latter acts as oxidant for CH $\boldsymbol{x}$ ($\boldsymbol{x}$=1-4) to form intermediate that will ultimately end with $CO_{(g)}$ .In the second pathway, CH_4 firstly is dehydrogenated to produce atomic H which subsequently activate the adsorbed CO_2 to produce COOH intermediate. Then, the decomposition of COOH results in CO and the oxidant OH as per below equation.

$$CO_2* + H* \rightarrow COOH * \rightarrow CO* + OH* \quad (15)$$

4.2.1 CO_2 direct activation

The adsorption of CO_2 on Ni_2Cu surface has been investigated at all possible sites. After geometry optimization, it has been found that CO_2 is physically adsorbed towards vacuum with weak adsorption energy of -0.03 eV in parallel to surface with C-Cu. This results agrees with Heiland[114] who has used both fast ion beam and fast molecular beam techniques to study CO_2 dissociation and found no chemisorbed CO_2 on Ni (111). Moreover, it also agrees with Zhu et al[36] and Xu et al[69] computational studies on Ni(111) and on Ni_2Fe surfaces respectively [33,64]. CO prefers to be adsorbed on Top^{Ni}, and O atom binds to FCC. The calculated adsorption energy is -1.51 for CO and -6.39 eV for atomic oxygen ,which indicate that Cu doping in Ni(111) network has improved atomic oxygen adsorption ability while weaken CO adsorption compared to both pure Ni(111) and Ni_2Fe surfaces respectively [33,64].

4.2.2 Hydrogen-induced CO_2 dissociation

As it has been described above, the hydrogen atoms released from CH_4 dissociation pathway may contribute or activate CO_2 activation. First, the CO_2 and hydrogen are co-adsorbed on Ni_2Cu surface to form an intermediate COOH with and activation energy barrier of 0.93 eV and exothermic reaction energy of -0.11 eV as shown in **Figure 17**. Then, the C-O bond is broken to reach a final state of co-adsorbed CO and OH on B^{2Ni} site with C-Ni bond length is 1.89A for CO and O-Ni bond length for OH .The activation energy barrier is found to be 0.43 eV and the reaction is exothermic with energy of -0.59 eV .

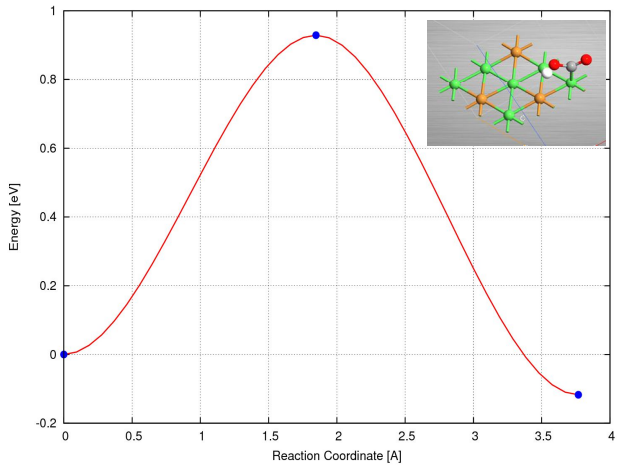

Figure 17 Activation energy profile of H-induced CO_2 activation .Gray frame show T.S. configuration

In previous studies of DRM on pure Ni (111) surface, CO_2 direct dissociation was found to be dominant with energy barrier of 0.67 eV[37] compared to 1.13 eV for the H-induced activation pathway[33]. Consequently, atomic oxygen was considered to be dominant oxidant of CH_x (x=1-4) intermediates. On the other hand, the Ni_2Cu surface has

reduced H-induced CO_2 dissociation from 1.13 eV to 0.93 eV. Thus, doping Cu in Ni (111) network has slightly favor the CO_2 hydrogenation process which will result in OH oxidant via $COOH^*$ intermediate dissociation. Comparing both CO_2 direct and induced activation pathways, one can say that H-induced CO_2 dissociation is more favorable than in Ni(111) case with both atomic oxygen and OH are participating as oxidants of CH_x (x=1-3) intermediates. Similar behavior has been reported for the Ni_2Fe surface as in **Figure 18**[67].

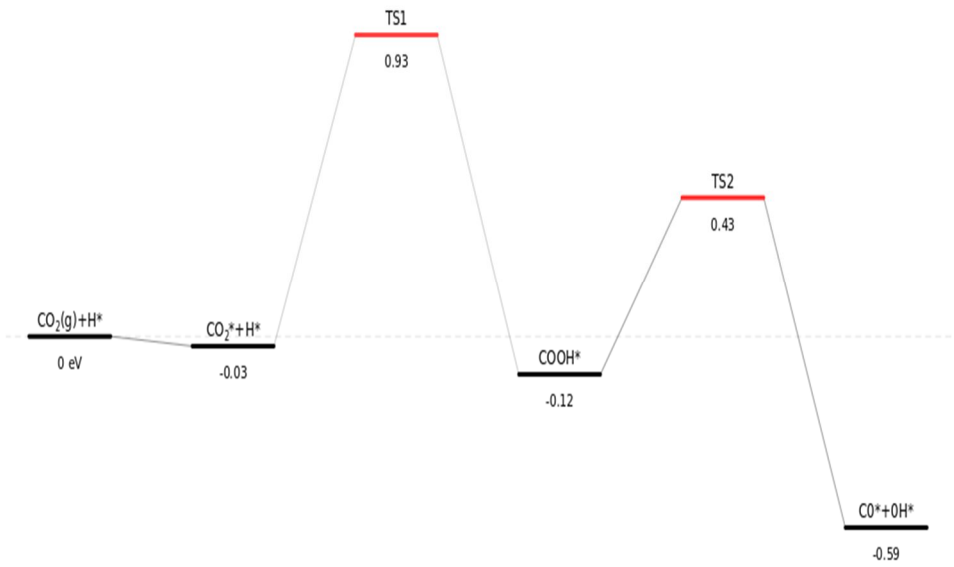

Figure 18 Activation energy profile for H-induced CO_2 dissociation.

4.3 Oxidation of C and CH

In the process of CH_4 dissociation to C and H, CH_x (x=0-3) may be coupled with either atomic oxygen or hydroxide species to produce $CH_xO(H)$. Our DFT calculations have shown that the CH_3 and CH_2 dehydrogenation reaction are more favorable due to

the facile energy barriers of 0.75 eV and 0.49 eV, respectively. In contrast, the CH dehydrogenation have significantly higher energy barrier of 1.41 eV and with the reverse reaction energically favored by 50% at activation energy barrier of 0.71 eV. Thus, coke formation due to CH decomposition is less favored in case of Ni_2Cu system compared to pure Ni (111) and Ni_2Fe surfaces which have less energy barriers of 1.33 and 1.36 eV, respectively. Moreover, only CH and C represent the most stable major intermediates that remain on the surface rather than the kinetically unstable CH_3 and CH_2 intermediates. To illustrate this assumption, all the possible oxidation of CH_x are systematically calculated. Among those calculations, it has been found that only C oxidation and CH oxidation are favorable.

4.3.1 Carbon elimination by C+O and C+OH reaction

C+O oxidation pathway has been found much more favorable with an activation energy barrier of **0.72 eV in an highly exothermic reaction energy of -2.17 eV** (compared to 1.59 eV and 1.58 eV in case of Ni(111) and Ni_2Fe, respectively) while C+OH have showed an activation barrier of **1.12** eV compared to 1.46 eV and 1.42 eV for Ni (111) and Ni_2Fe surfaces, respectively. Moreover, the reverse reaction of CO→C+O has to overcome 2.89 eV activation energy barrier which is clearly in favor of carbon elimination. This breakthrough indicates that this particular oxidation reaction is accelerated on Cu enriched surface with Cu change the surface properties to enhance carbon elimination by atomic oxygen and even by OH species at lesser extent that cannot be ignored too **Figure 19** and **Figure 20**.

As will be explained later, the temperature will play crucial role to enhance these oxidation steps. From these results, one can conclude that doping Cu in the Ni (111) have reduced coke formation by both increasing the activation energy barrier of CO and CH dissociation while improving carbon elimination by both atomic oxygen and OH species. These outstanding results overcoming both Ni(111) and Ni_2Fe in terms of coke resistance and agrees with both previous computational and experimental studies[69, 82, 85,115].

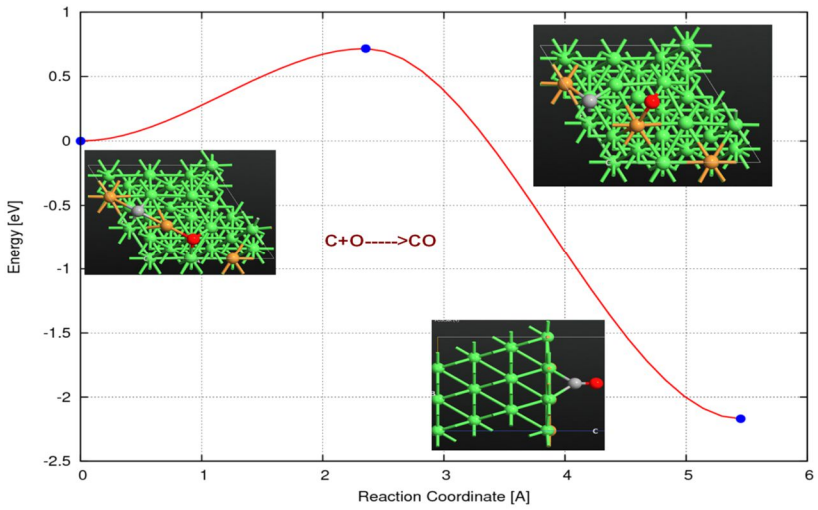

Figure 19 Coke removal via atomic oxygen has smallest energy barriers of all other oxidation reactions. Black Frames are showing initial state, T.S. and final state.

Figure 20 Comparative activation energy profiles of C+O oxidation reaction for Ni_2Cu (red) and Ni_2Fe (black) surfaces. It shows that carbon elimination is improved more than twice.

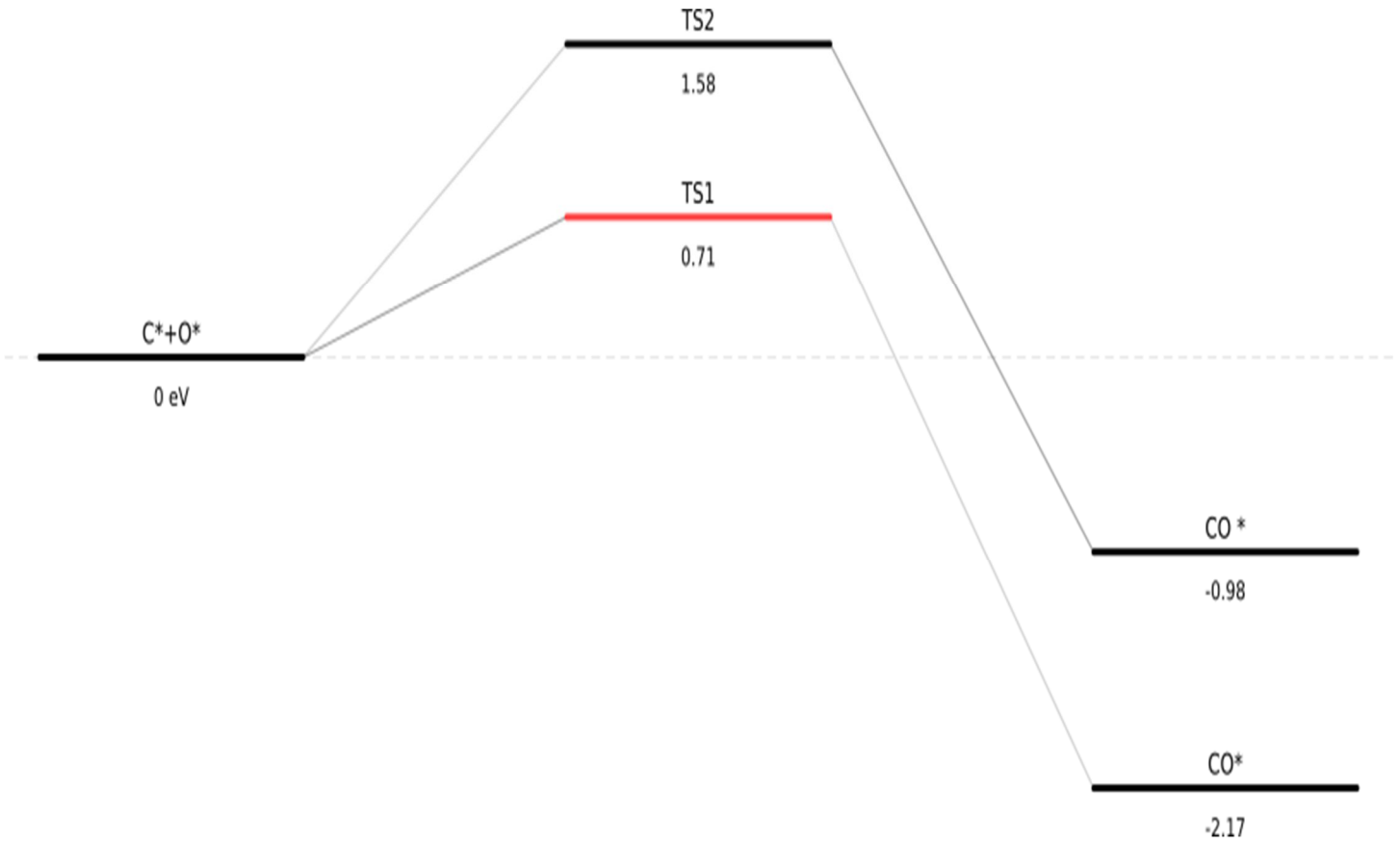

4.3.2 CH+O and CH+OH reactions

The oxidation of CH by atomic oxygen generated from CO_2 direct dissociation begins from co-adsorption of CH on FCC and oxygen atom on HCP with one Cu bridging between the two species. At transition state, atomic oxygen moves to B^{NiCu} site with Ni-O distance of 1.97˚A and Cu-O distance of 2.01˚A while CH settles at B^{2Ni} site with Ni-C distance of 1.86˚A and 1.81 ˚A. It has been calculated that the energy barrier of that step is only 1.06 eV which is significantly lower by 0.47 eV and by 0.78 eV than that of pure Ni (111) and Ni_2Fe surface respectively. Similarly, CH and OH are co-adsorbed at adjacent FCC and B^{2Ni}sites, then the intermediate CHOH is formed by overcoming energy barrier of only 1.08 eV compared to 1.48 eV and 1.42 in case of pure Ni (111) and Ni_2Fe, respectively as in **Figure 21**.

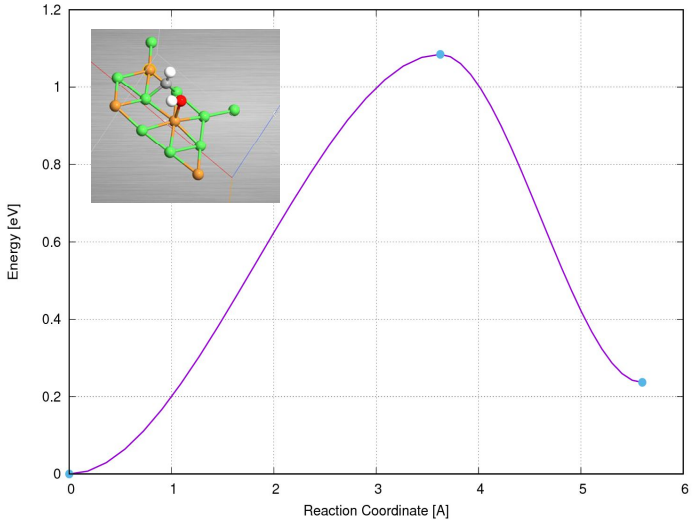

Figure 21 Activation energy profile of CH oxidation by OH.OH is effective oxidant that helps skipping CH dissociation. Gray frame is showing T.S. configuration where OH is adsorbed on Top^{Cu} while CH adsorbed on Top^{Ni}.

4.3.3 CHO (H) and COH decomposition

The stable CHOH configuration involves CHOH located at B^{2Ni} site with equal C-Ni distances of 1.95 ˚A. The subsequent CHOH* have two possible pathways. The first pathway involves the dissociation via CHOH*→CHO*+H* at activation energy barrier of 0.60 eV. Then the produced CHO is facile to dissociate to form CO and atomic H at energy barrier of 0.18eV as in **Figure 22** .

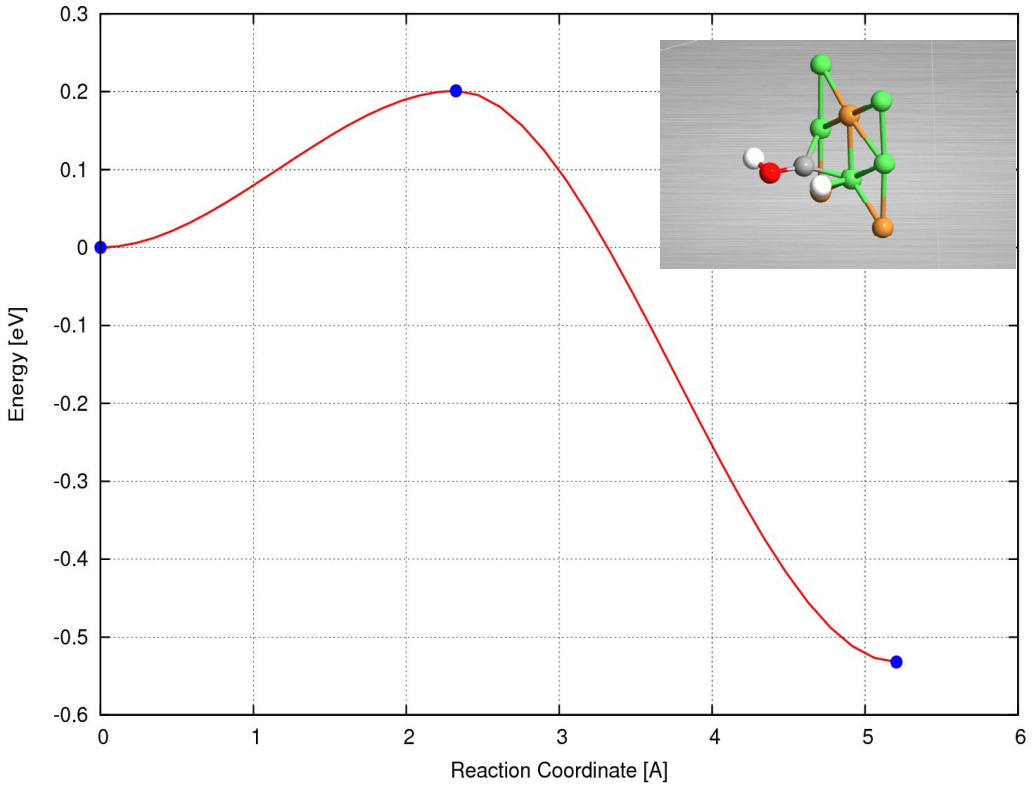

Figure 22 Activation energy profile of CHOH favorable dissociation to form COH*+H*.Gray frame is showing T.S. configuration.

The second pathway is going through formation of COH* and H* after overcoming a facile energy barrier of only 0.20 eV and then the COH* dissolves to CO and atomic H at energy barrier of 1.09.From above calculations, one can conclude that CH oxidation by atomic oxygen and OH oxidants are very competitive with a minute energy barrier difference (1.06 and 1.08 eV ,respectively) which distinguishes Ni_2Cu system from Ni(111) and Ni_2Fe by the active participation of OH as oxidant as in **Figure 23**[33,64]. Moreover, it has been found that in spite of the slightly lower activation barrier of CH oxidation by atomic oxygen, CH oxidation by OH shows higher rate constant at reaction temperature from 800-1000K as it will be elaborated later.

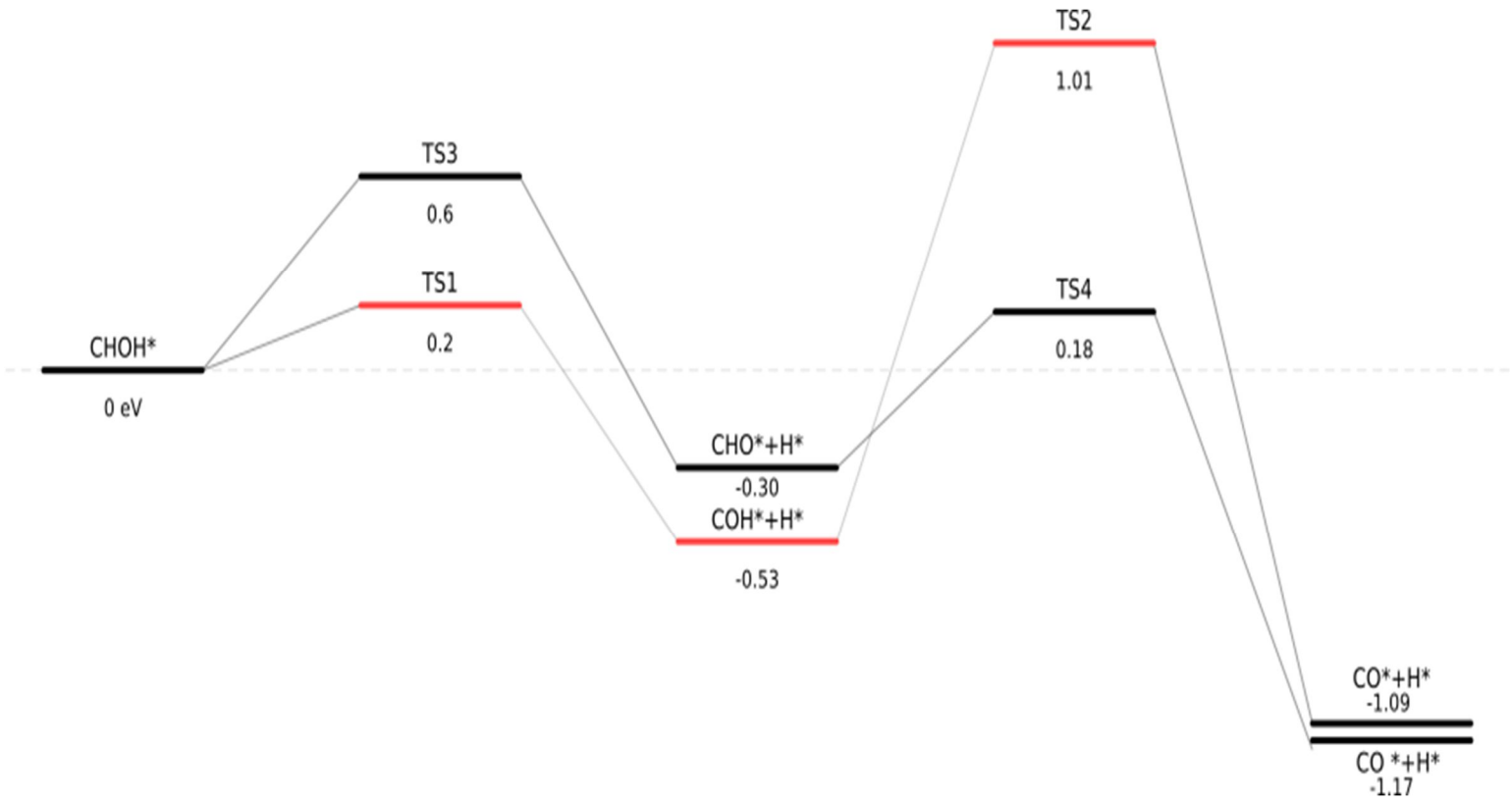

Figure 23 Activation energy profile of different CHOH* dissociation pathways.

4.4 H_2 and H_2O formation

The reaction of H* +H* →H_2 (g) requires activation energy barrier of **0.71 eV** with endothermic reaction energy of **0.57 eV**. The formed H_2 (g) is physically adsorbed on catalyst surface with adsorption energy of -0.016 eV which in-along with endothermicity in the high reaction temperatures- favor of product formation. Thus, H_2 (g) product formation via Ni_2Cu catalyst is more facile than pure Ni(111) and Ni_2Fe which possess relatively higher energy barrier of 0.92 eV or even 1.18 eV, respectively as in **Figure 24**[33,64].

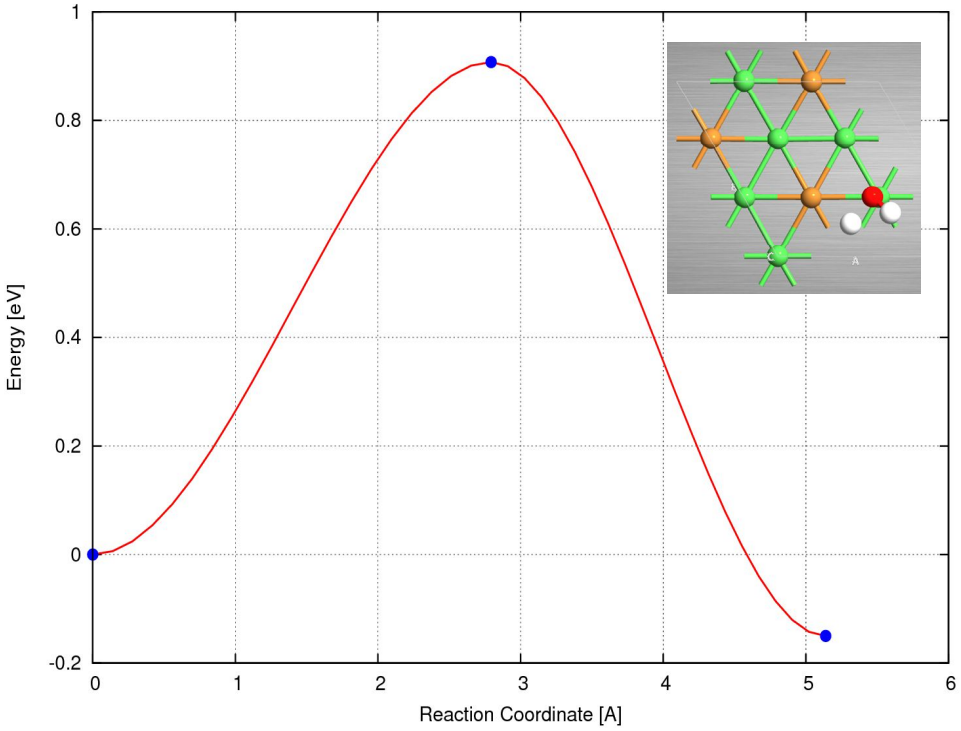

Figure 24 H_2O formation via OH*+H* reaction. The weakly adsorbed H_2O may physically remove coke from catalyst surface in DRM elevated temperatures (steam). Gray frame is showing T.S.

Table 3 Calculated activation energies for all forward ($E_{a,f}$) , reverse ($E_{a,r}$) and enthalpy (ΔH_f) of elementary reaction involved in dry reforming of methane.

Reaction	$E_{a,f}$* (eV)	ΔH_f** (eV)	$E_{a,r}$*** (eV)
CH_4-->CH_3+H	1.30	0.78	0.52
CH_3-->CH_2+H	0.75	0.33	0.42
CH_2-->CH+H	0.49	-0.06	0.55
CH-->C+H	1.40	0.69	0.71
C+O-->CO	0.72	-2.17	2.89
CH+O-->CHO	1.06	-0.30	1.36
CHO-->CO+H	0.18	-1.17	1.35
C+OH-->COH	1.13	-0.95	2.07
H+H-->H_2	0.73	0.57	0.16
CH+OH-->CHOH	1.08	0.24	0.84
CHOH-->CHO+H	0.60	-0.31	0.91
CO_2+H-→COOH	0.93	-0.12	1.05
COOH-->CO+OH	0.43	-0.59	1.02
O+H-->OH	0.94	-0.24	1.18
H+OH-->H_2O	0.91	-0.15	1.06
CO_2-->CO+O	1.69	0.48	1.21
CH_3+O-->CH_3O	1.37	-0.22	1.59
CH_2+O-→CH_2O	0.76	-0.43	1.19
CHOH-→COH+H	0.20	-0.53	0.73
COH-->CO+H	1.01	-1.09	2.10
CH_3+OH-->CH_3OH	1.60	-0.14	1.74
CH_2+OH-->CH_2OH	0.78	-0.10	0.88
CH_3O-->CH_2O+H	0.96	0.57	0.39
CH_2OH-->CH_2O+H	0.75	-0.07	0.82
CH_2OH-->CHOH+H	0.92	0.42	0.50
CH_3OH-->CH_3O+H	4.29	0.01	4.28
CH_3OH-→CH_2OH+H	2.46	1.39	1.10

*,**,*** ZPE corrections are not included

Table 3 summarizes the calculated energy barriers for all possible elementary reactions involved in DRM. For H_2O formation, the adsorbed H and O atoms are reacting to produce OH with energy barrier of 0.94 eV and exothermic reaction energy of -0.24 eV. Finally, the formed OH reacts exothermically with H with similar activation energy

barrier of around 0.91 eV and reaction energy of -0.15 eV. These two steps are favored energetically than similar steps on pure Ni (111) surface and Ni_2Fe (111) surfaces. The H_2O formed is physically adsorbed at the surface with adsorption energy of -0.06 eV. In elevated temperature of DRM, this H_2O may participate in physical removal of coke deposition on the catalyst surface.

4.5 Effect of Cu and temperature on carbon deposition resistance

One of the drawbacks of DFT is that calculations follow ***zero temperature approach***. The calculations reflect the condition where atoms are localized at "minimum energy" positions at 0 K. To overcome this problem, a complete vibrational analysis is performed on the elementary reaction. It is well-know that atoms in material are vibrating around their equilibrium positions at different temperature. These vibrations can be measured experimentally by spectroscopic methods and therefore have a great importance in DFT.

Calculation of vibrational frequencies has double benefit. First, it can confirm the transition state configuration as well as the activation energy barrier. One striking feature of these frequencies is that at the transition state, one of them is imaginary (i.e., the eigenvalue associated with this vibrational mode is negative). The reason behind that is the transition state is a point on the potential energy surface that is a minimum in all directions but one. Second benefit is that it can be used to confirm calculate the rate constant via partion function or vineyard formula. The later is the crucial central step in developing microkinetic model of the overall reaction and identify atomistic model as in **Figure 25**[116].

In that context, we will utilize the calculated vibrational frequencies to evaluate the rate constant from the confirmed transition states with focus on the role of Cu doping and temperature on coke deposition resistance.

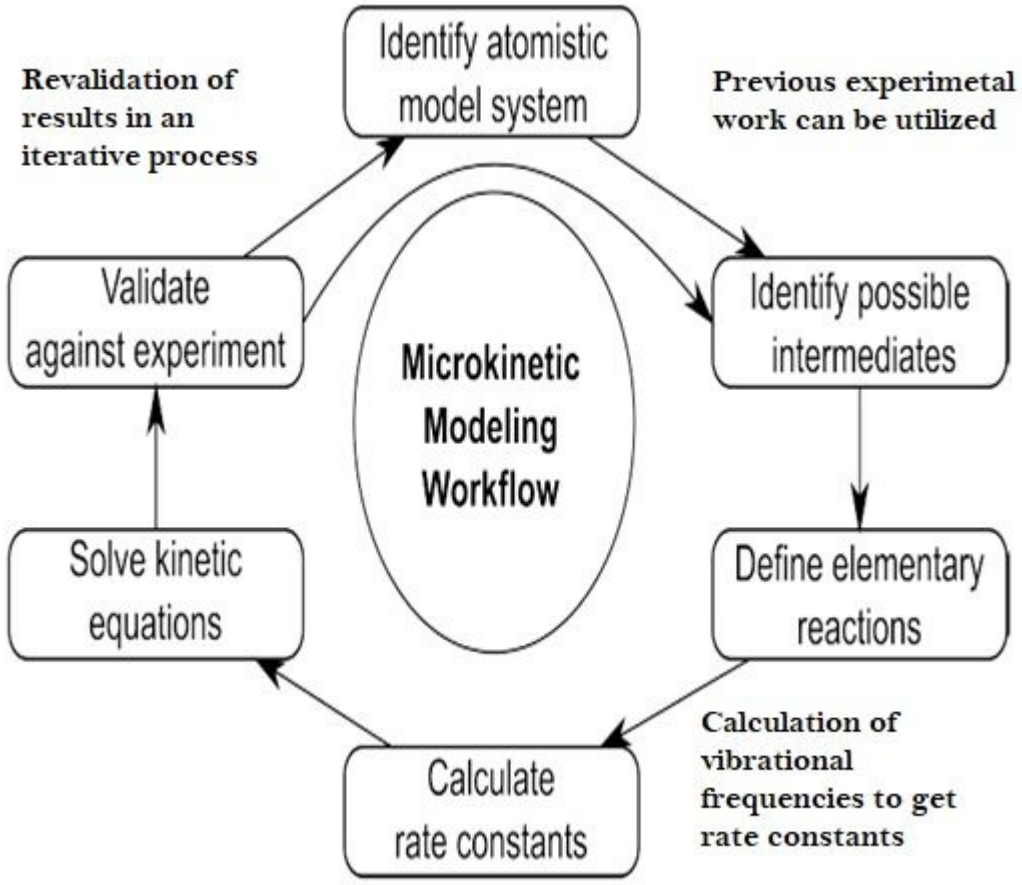

Figure 25 Illustration of workflow for constructing a microkinetic model adapted from[116].

Under realistic conditions, DRM is highly endothermic which require temperatures as high as 800-1000 K to obtain reasonable conversion [117] and coke

resistance [39].So in order to understand the effect of temperature and Cu doping on coke deposition resistance ,complete vibrational analysis for the involved elementary reaction is performed to calculate the rate constants at that temperature range. Coke deposition can be from two main source: CH4 and CO2.For carbon formation from CH_4,CH dissociation have to overcome 1.40 eV. This carbon can be easily oxidized by atomic oxygen with energy barrier 0.71 eV only. Moreover, more importantly, CH oxidation pathway will transfer CH to CO via CHO skipping carbon formation from CH_4 dissociation pathway. Thus, the rate constant ratio of CH oxidation pathway to C oxidation pathway will determine carbon deposition from CH_4 route. As this ratio becomes high, then carbon formation is reduced[37].

Regarding CO_2, carbon formation faces a very high energy barrier of 2.89 eV. So, dissociation of CO into C and O is highly unfavorable on Ni_2Cu surface which diminish coke formation from CO_2 route. **Table 4** shows rate constants k(s^{-1}) on Ni_2Cu surface at different temperatures for reactions involved in carbon elimination and deposition.

In general, k of C+O (OH) increases with the increasing temperature. The results confirm that carbon deposition from CO is negligible due to the very small k values. In addition, CH is dissociation rate constant is less than that of carbon oxidation either by atomic oxygen or by OH species. With increasing temperature, k_{CH}/k_C(O) increase while k_{CH}/k_C(OH) decreases.

Table 4 Rate Constant k(S^{-1}) on Ni_2Cu surface at different temperatures.

Ni_2Cu Surface	800K	850K	900K	950K	1000K
CO→C+O	4.36E-07	5.11E-06	4.56E-05	3.23E-04	1.88E-03
CH -->C+H	1.18E+05	3.90E+05	1.13E+06	2.92E+06	6.88E+06
C+O—>CO	2.43E+08	4.50E+08	7.74E+08	1.25E+09	1.95E+09
C+OH-->COH	5.75E+06	1.50E+07	3.53E+07	7.59E+07	1.51E+08
CH+O-->CHO	6.01E+06	1.49E+07	3.32E+07	6.83E+07	1.31E+08
CH+OH-->CHOH	3.28E+07	8.27E+07	1.88E+08	3.93E+08	7.62E+08
$k_{CH}/k_{C(O)}$	0.02	0.03	0.04	0.05	0.07
$k_{CH}/k_{C(OH)}$	5.70	5.50	5.33	5.18	5.05

Figure 26 shows temperature effect on carbon elimination. C+O possesses the highest rate constant of all carbon elimination reactions followed by CH+OH while C+OH and CH+O have comparable rate constants. In addition, one can conclude that OH is dominant oxidant for CH while atomic oxygen is dominant for coke removal at different temperature. From one hand, this reveals the easy removal of coke deposition by atomic oxygen at the higher temperature range. On the other hand, it also reveals the importance of OH species role to bypass the coke formation step from CH dissociation especially at the lower to medium temperature range where $k_{CH}/k_{C(OH)} >> k_{CH}/k_{C(O)}$.

Comparing these results to Zhang et al work[70],carbon elimination via C+O reactions in Ni_2Cu>NiCu (1:1)>pure Ni(111) .This suggests that carful decoration of Ni-Ni surface with Cu atoms will enhance the carbon elimination by C+O reaction while reducing the carbon deposition via CH dissociation. Higher Cu/Ni ratio is expected to

suppress the catalyst activity probably as it occupies Ni active site. These results agree with experimental results[69,82,118].

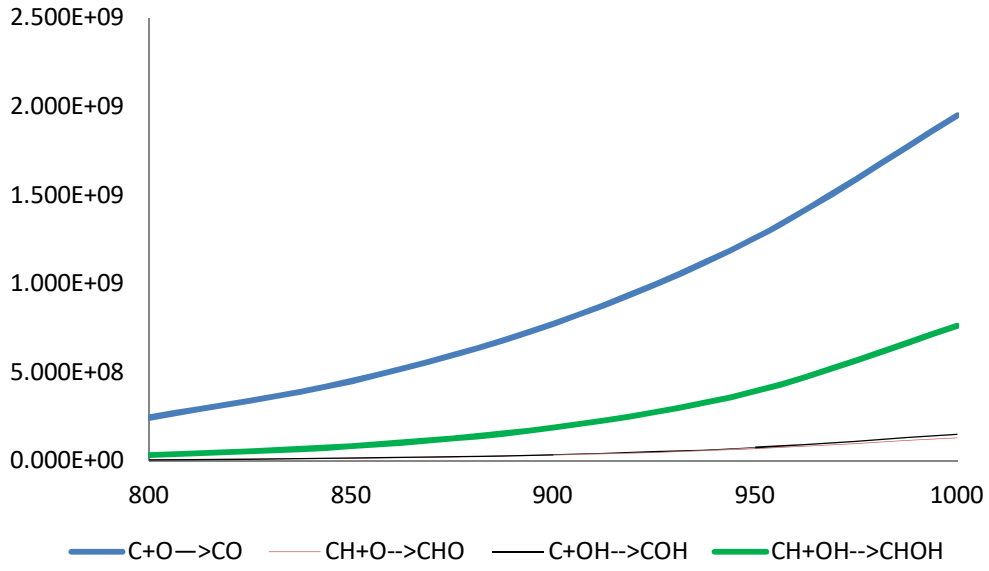

Figure 26 Rate constant values of coke removal reactions on different temperatures.

Moreover, the reaction proceeds, it is expected to show more stability as rate of carbon elimination by both OH and atomic oxygen will be much higher of carbon deposition via CH dissociation. This periodic cycle of carbon deposition and elimination result in catalyst stability as explained in **Figure 27**.

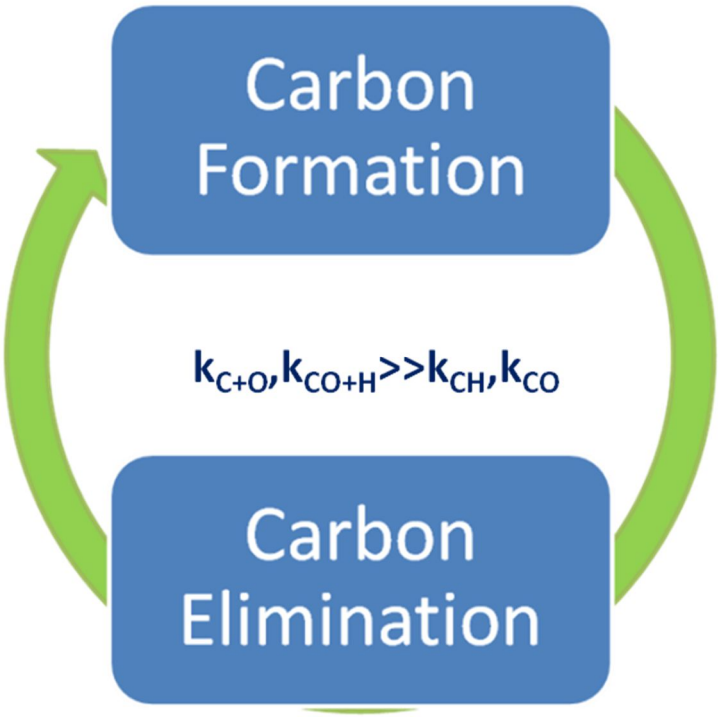

Figure 27 Periodic cycle of carbon deposition and elimination results in is Ni_2Cu catalyst stability

Reaction	Frequencies (cm^{-1})	$ZPE^{T.S}$ (eV)
CH4-->CH3+H	**819.53*,** 59.11 ,108.04 ,132.75 ,261.32 ,362.45 , 673.55 ,789.46 ,1143.10 ,1359.84 ,1394.47 ,1623.37 ,2969.78 ,3062.81 ,3087.85	1.06
CH3-->CH2+H	**918.70** ,2983.18 ,2933.26 ,1682.49 ,1339.03 , 895.72, 710.83, 554.02, 507.44, 325.13, 232.66, 117.91	0.76
CH2-->CH+H	**869.34** ,165.36 ,274.50 ,441.62 ,596.77 ,659.66 ,887.05 ,1547.77 ,3043.56	0.47
CH-->C+H	**961.56** ,258.61 ,388.83 ,532.72 ,569.96 ,1308.36	0.19
C+O-->CO	**219.59 ,**399.37 ,420.94 ,514.03 ,553.52 ,614.10	0.16
CH+O-->CHO	**464.03** ,129.67 ,270.90 ,384.45 ,465.37 ,584.49 ,692.61 ,910.96 ,3069.77	0.40
CHO-->CO+H	**328.43** ,71.95 ,84.59 , 190.42,303.42 ,601.96 ,1038.61 ,1570.87 ,2522.31	0.40
C+OH-->COH	**181.06** ,72.61 ,186.82 ,324.76 ,378.84 ,576.60 ,589.12 ,640.27 ,3676.65	0.40
H+H-->H2	**841.83 ,**165.81 ,246.70 ,350.07 ,1632.59 ,1880.40	0.27
CH+OH-->CHOH	**157.86** ,90.71 ,99.16 ,161.57 ,174.99 ,373.96 ,539.84 ,604.36 ,621.58 ,813.22 ,2939.62 ,3658.00	0.62
CHOH-->CHO+H	**1293.53** ,129.26 ,162.25 ,188.72 ,209.12 ,321.76 ,546.69 ,692.61 ,850.51 ,952.32 ,1146.87 ,2771.89	0.49
CO2+H-→COOH	**1351.94** ,87.91 ,101.57 ,144.06 ,240.08 ,303.05 ,469.25 ,530.16 ,683.00 ,892.49 ,1150.57 ,1545.00	0.38
COOH-->CO+OH	**178.76 ,**65.60 ,125.85 ,178.29 ,204.22,317.52 ,382.05 ,426.69 ,542.31 ,762.23 ,1830.49 ,3509.01	0.52
O+H-->OH	**1199.07** ,240.02 ,246.75 ,324.31 ,468.52 ,1492.46	0.17
H+OH-->H2O	**624.65** ,97.25 ,150.44 ,337.45 ,407.75 ,566.99 ,745.44 ,913.98 ,3652.67	0.43

Table 5 Vibrational frequencies and Zero-point energy correction of T.S. of dominant elementary reactions.
*Bold numbers are the imaginary frequencies that confirm the T.S

4.6 Dominant reaction pathways and rate-limiting step

Based on DFT calculations of activation energy barriers of DRM over Ni_2Cu which are confirmed by vibrational frequencies as **Table 5**, the most dominant pathways can be predicted.CH_4 undergoes successive dehydrogenation steps ,among them CH_3 and CH_2 dissociation are the more facile with energy barrier of 0.75 eV and 0.49 eV respectively. Moreover, oxidations of these species either by atomic oxygen or OH are not favored energetically due to higher energy barrier of 1.37 eV and 1.6 eV in case of CH_3 and 0.76 eV and 0.78 in case of CH_2 oxidation, respectively. Consequently, the CH_4 dissociation will result in that CH, C and H at lesser extent as the main intermediates.

As discussed separately above, CH showed 3 major pathways as follow

I. $CH^* \rightarrow C^* + H^*$

II. $CH^* + O^* \rightarrow CHO^* \rightarrow CO^* + H^*$

III. $CH^* + OH^* \rightarrow CHOH^*$

Having to overcome significantly higher energy barrier 1.41 eV, CH dissociation is the major source of coke formation have become quite difficult due to doping Cu into Ni (111) network. Moreover, coke formation from CO dissociation has been found energetically and kinetically unfavorable. Moreover, CH dissociation has been found the rate-limiting step of the reaction and expected to determine the overall rate of reaction.

For CH* oxidation, both oxidation pathways II and III are very competitive with oxidation by atomic oxygen is slightly favored over OH oxidation with energy barrier of 1.06 eV. However, kinetic data favors the CHOH* formation based on vibrational analysis and rate constant. Regarding CHOH*, the most favored pathway goes through

formation of COH* with activation energy barrier of 0.20 eV which further dissociate to CO* and H*.

Looking at coke elimination, oxidation by atomic oxygen is more favorable with only 0.71 eV energy barriers to overcome. As for H* intermediate, H* + H* $\rightarrow H_2$* is the most favored pathway.

Regarding CO_2 activation pathways are possible, CO_2 direct dissociation to form CO and O (pathway I) and H-induced CO_2 formation through intermediate COOH* which in turn dissociate to CO* and OH* (pathway II) .Pathway II has been found to be more favorable with an energy barrier of 0.93 eV which suggests that doped Cu atoms have promoted H-induced CO_2 activation pathway which results in formation of both O and OH oxidants responsible for CH and C elimination on the Ni_2Cu surface. Rate constant calculations have revealed carbon oxidation by atomic oxygen is the more favorable elimination reactions followed by CH+OH while C+OH and CH+O have comparable rate constants. The overall mechanism is summarized in **Figure 28**

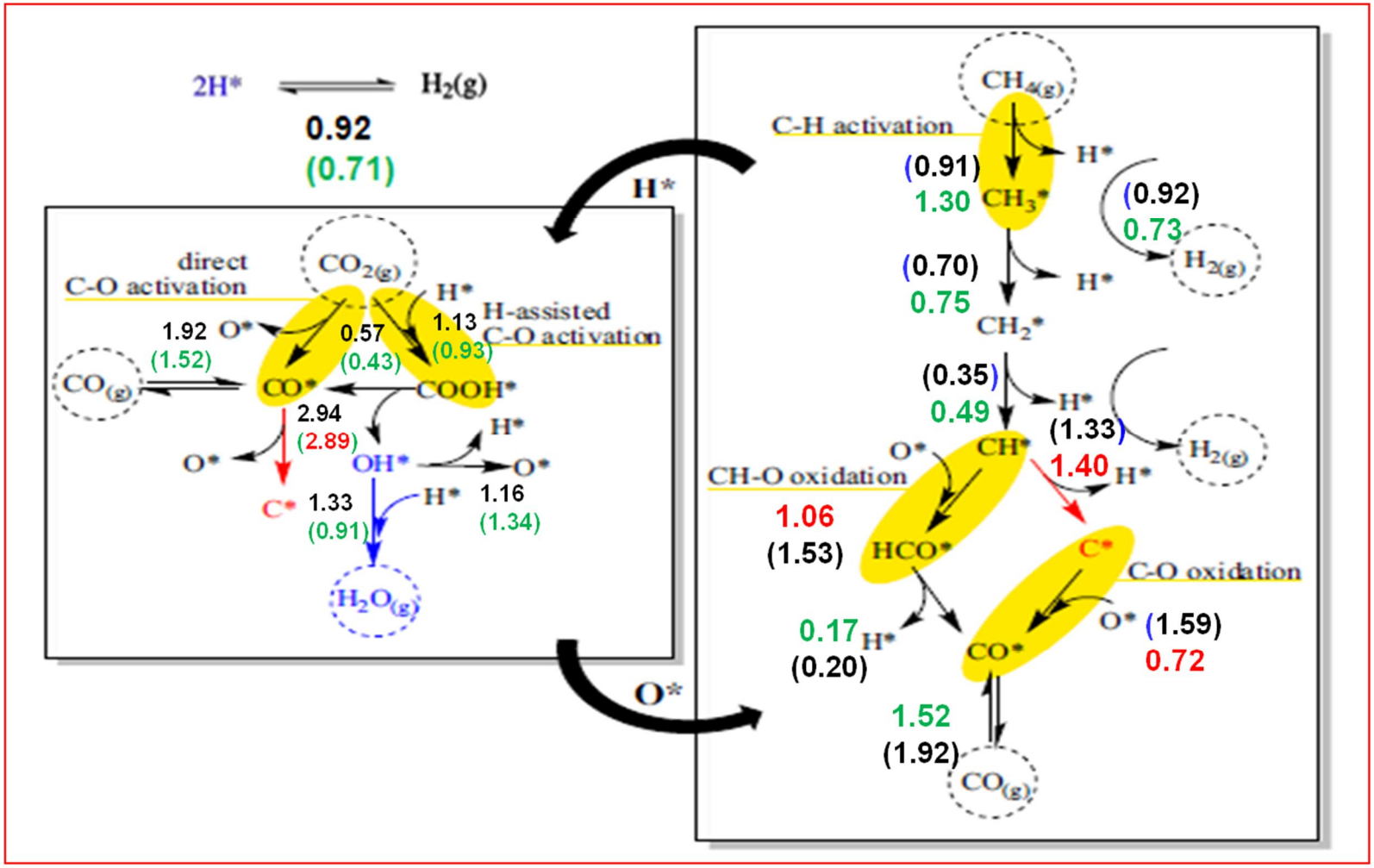

Figure 28 Dominant pathways energy barriers in eV. For comparison, E_a in black is for Ni (111), green is for Ni_2Cu surface while red color values are for carbon deposition/elimination steps on Ni_2Cu surface adapted from [119]..

5 CONCLUSION, RECOMMENDATIONS AND FUTURE WORK

5.1 Conclusion

To summarize, this study aimed to get mechanistic understanding of dry reforming of methane (DRM) on Ni_2Cu surface on the molecular level utilizing density functional theory (DFT) calculations.

All elementary reactions steps are covered comprehensively which include CH_4 dehydrogenation, CO_2 activation, CH and C oxidation via atomic oxidation and OH. First, the adsorption different species suggested the most stable configurations and the corresponding adsorption energies. Then, the detailed mechanism has been investigated using climbing nudged elastic band method (cNEB) followed by dimer method to locate the elementary reaction saddle points. The results pointed that CH_4 and CH dissociation energy barrier have been significantly increased in presence of doped Cu in Ni-Ni network. Moreover, CH dissociation has been found the rate-limiting step of the reaction with 1.41 eV energy barrier which suggests significant improvement in regarding carbon deposition inhibition compared to similar reactions on Ni (111) and Ni_2Fe surfaces.

In addition, it has been found that in presence of Cu, the coke elimination via oxidation have been not only improved remarkably in case of atomic oxygen as oxidant but also showed active participation of OH species. The later have been clearly seen in the difference of energy barriers of CH oxidation by atomic oxygen and that one by OH species which was only 0.02 eV. Among the C/CH oxidation pathways, C* + O* → CO (g) has been found the most favorable with energy barrier of 0.71 eV which is almost less

than half of that of Ni (111) and Ni_2Fe for the similar reaction. Furthermore, easier H_2O (g) formation can physically assist to halt coke deposition.

Comparing these results to Zhang et al work[70],carbon elimination via C+O reactions in Ni_2Cu>NiCu (1:1)>pure Ni(111).This suggests that carful decoration of Ni-Ni surface with Cu atoms will enhance the carbon elimination by C+O reaction while reducing the carbon deposition via CH dissociation. Higher Cu/Ni ratio is expected to suppress the catalyst activity probably as it occupies Ni active site. These results agree with experimental results in literature[69,82,118] and our group experimental work .

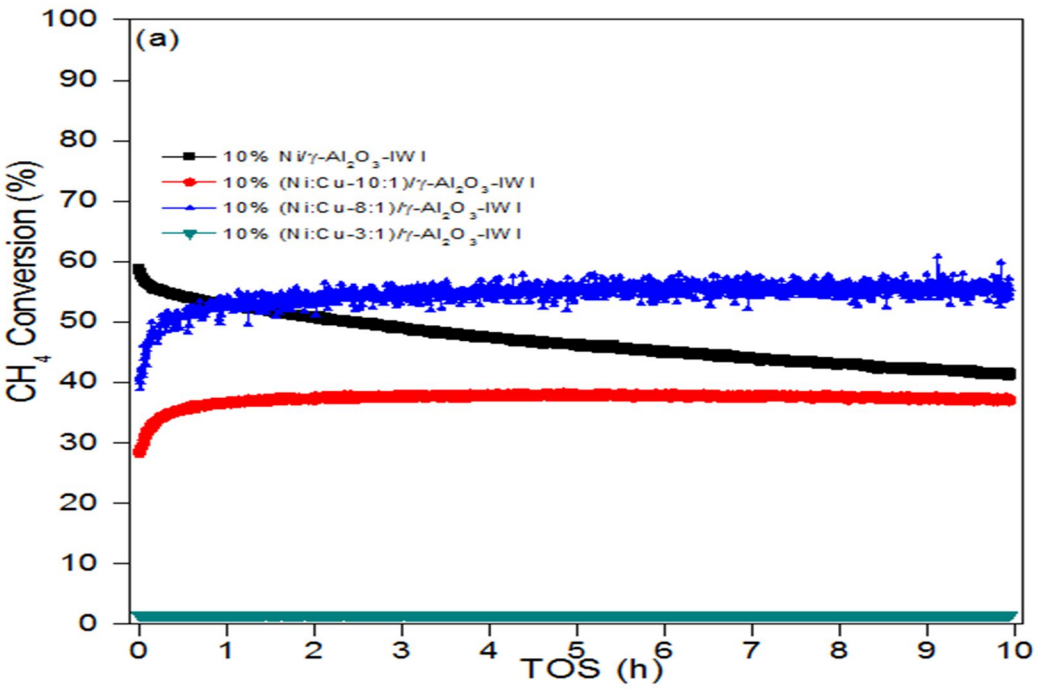

Figure 29 CH_4 conversion for DMR on Ni(111) and different Ni-Cu modified catalyst. Medium Ni-Cu catalyst (in blue) is showing sustained conversion over TOS of 10 h reprinted with permission from our research group.

From experimental and DFT calculation, it has been found that Ni (111) catalyst which shows higher initial activity and later drastic drop in catalyst activity and conversion due to coke deposition on catalyst surface[31]. On the other hand, the proposed Ni_2Cu catalyst is expected to show less initial activity due to the relatively higher CH_4 dissociation steps energy barriers. However, as the reaction proceeds to equilibrium conversion, this "slow down" behavior of initial conversion will result in sustained activity is for prolong period due to timely coke removal as in **Figure 29**. In addition, the CO_2 dissociation is easily activated via H-induced pathway. Coupled with the facile dissociation of COH*, CHOH* and COOH* intermediates, the reaction is expected to maintain sustainable CO_2 conversion as **Figure 30**.

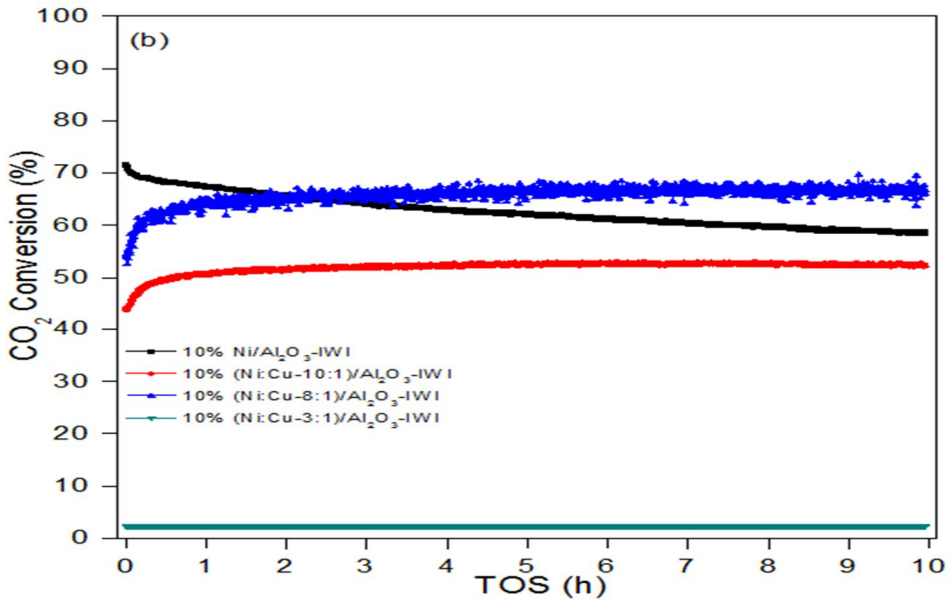

Figure 30 CO_2 conversion for DMR on Ni(111) and different Ni-Cu modified catalyst. Medium Ni-Cu catalyst (in blue) is showing sustained conversion over TOS of 10 h reprinted with permission from our research group.

Last, it is expected to have a stable H_2/CO ratio near unity due to two main reasons: first, CH oxidation is more favorable than CH dissociation and ultimately from CO and second is that the relatively slow CH_4 dissociation will control the atomic H* species which end up with H_2 (g) formation as in **Figure 31**.

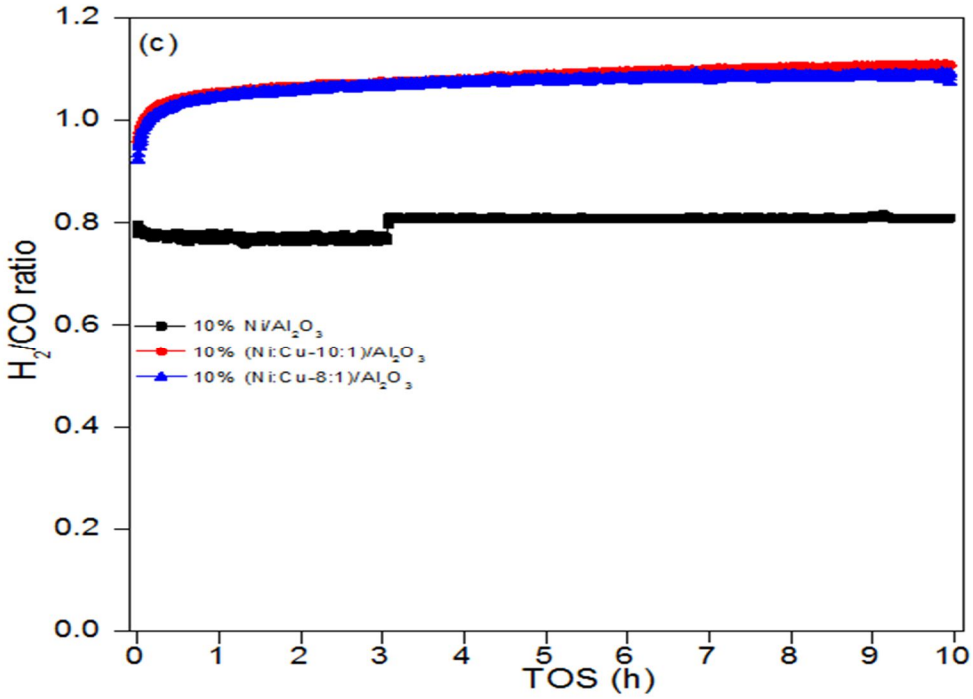

Figure 31 H_2/CO ratio for DMR on Ni (111) and different Ni-Cu modified catalyst. Medium Ni-Cu catalyst (in blue) is showing sustained conversion over TOS of 10 h reprinted with permission from our research group.

To conclude, it is expected that once carbon deposition occurs on Ni_2Cu surface, the coke is timely removed as rate of carbon elimination-by different oxidation reaction- will be much higher of carbon deposition. This efficient periodic cycle of carbon deposition and carbon elimination contributes to more stable catalytic performance that

explains the experimental results that Ni-Cu bimetallic catalysts have outstanding catalytic performance and excellent carbon deposition resistance in DRM.

5.2 Recommendations and future work

The DFT calculations suggested outstanding carbon-resistance ability which leads to stable prolonged activity for Ni_2Cu catalyst. It represent cheap and environmental friendly alternative for noble metal-based catalysts. . Computationally, these results also can be solid basis to build a detailed microkinetic model for DRM over Ni_2Cu reaction. It is also recommended to examine the possible role of different supports for the suggested catalyst. Moreover, it is recommended that these results are confirmed by experimental work to identify the optimum amount of Cu doping in the Ni-Ni network in an iterative approach as **Figure 32**. In that direction, it also suggested the different supports are included in the calculation to examine their role in the reaction mechanism. Catalyst regeneration and disposal process need to be investigated to further examination of its feasibility.

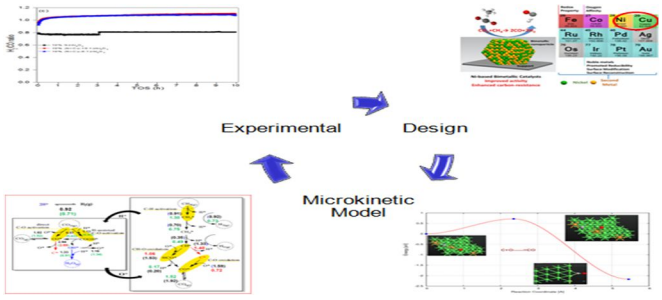

Figure 32 Integrated approach of Ni_2Cu catalyst Design

REFERENCES

1. Emily Tillett. Watch: Macron address to Congress today live stream and updates during speech - CBS News. Apr 25, 2018. https://www.cbsnews.com/live-news/french-president-emmanuel-macron-address-to-congress-today-live-updates-stream-2018-04-25/. Published 2018. Accessed August 28, 2018.

2. Aresta M, Dibenedetto A. Utilisation of CO2 as a chemical feedstock: opportunities and challenges. *Dalt Trans*. 2007;0(28):2975. doi:10.1039/b700658f

3. Song C. Global challenges and strategies for control, conversion and utilization of CO2 for sustainable development involving energy, catalysis, adsorption and chemical processing. *Catal Today*. 2006;115(1-4):2-32. doi:10.1016/J.CATTOD.2006.02.029

4. Kondratenko E V., Mul G, Baltrusaitis J, Larrazábal GO, Pérez-Ramírez J. Status and perspectives of CO2 conversion into fuels and chemicals by catalytic, photocatalytic and electrocatalytic processes. *Energy Environ Sci*. 2013;6(11):3112. doi:10.1039/c3ee41272e

5. Guo J, Hou Z, Gao J, Zheng X. Syngas production via combined oxy-CO2 reforming of methane over Gd2O3-modified Ni/SiO2 catalysts in a fluidized-bed reactor. *Fuel*. 2008;87(7):1348-1354. doi:10.1016/J.FUEL.2007.06.018

6. Hironori Arakawa ▪, Michele Aresta †, John N. Armor ‡, et al. Catalysis Research of Relevance to Carbon Management: Progress, Challenges, and Opportunities. 2001. doi:10.1021/CR000018S

7. Hansen J, Sato M, Ruedy R. Perception of climate change. *Proc Natl Acad Sci U S A*. 2012;109(37):E2415-23. doi:10.1073/pnas.1205276109

8. Encyclopedia of Global Warming and Climate Change Globalization. 2008. doi:10.4135/9781412963893

9. Safi MA, Kotb M, Yiğiterhan O, et al. Geographical distribution of air pollution in Doha, Qatar View project Monitoring of new particles formation in ambient air View project Geographical distribution of air pollution in Doha, Qatar. 2018. doi:10.13140/RG.2.2.12822.45129

10. Alfoldy B, Kotb M, Yigiterhan O, Elobaid EA, Safi M. BTEX, nitrogen oxides, ammonia and ozone concentrations at traffic influenced urban sites in an arid environment. *20th EGU Gen Assem EGU2018, Proc from Conf held 4-13 April 2018 Vienna, Austria, p6628*. 2018;20:6628.

http://adsabs.harvard.edu/abs/2018EGUGA..20.6628A. Accessed September 8, 2018.

11. Al-Yaeeshi AA, Al-Ansari T, Govindan R. The potential for carbon dioxide capture and utilization within the State of Qatar. *Comput Aided Chem Eng*. 2018;43:1499-1504. doi:10.1016/B978-0-444-64235-6.50261-8

12. Afzal S, Sengupta D, Sarkar A, El-Halwagi M, and, Elbashir N. Optimization Approach to the Reduction of CO_2 Emissions for Syngas Production Involving Dry Reforming. *ACS Sustain Chem Eng*. 2018;6(6):7532-7544. doi:10.1021/acssuschemeng.8b00235

13. Valderrama G, Kiennemann A, de Navarro CU, Goldwasser MR. LaNi1-xMnxO3 perovskite-type oxides as catalysts precursors for dry reforming of methane. *Appl Catal A Gen*. 2018;565:26-33. doi:10.1016/J.APCATA.2018.07.039

14. Tillmann L, Schulwitz J, van Veen A, Muhler M. Dry Reforming of Methane at High Pressure in a Fixed-Bed Reactor with Axial Temperature Profile Determination. *Catal Letters*. 2018;148(8):2256-2262. doi:10.1007/s10562-018-2453-x

15. le Saché E, Pastor-Pérez L, Watson D, Sepúlveda-Escribano A, Reina TR. Ni stabilised on inorganic complex structures: superior catalysts for chemical CO 2 recycling via dry reforming of methane. *Appl Catal B Environ*. 2018;236:458-465. doi:10.1016/j.apcatb.2018.05.051

16. Muraza O, Galadima A. A review on coke management during dry reforming of methane. *Int J Energy Res*. 2015;39(9):1196-1216. doi:10.1002/er.3295

17. Uykun Mangaloğlu D, Baranak M, Ataç Ö, Atakül H. Effect of the promoter presence in catalysts on the compositions of Fischer–Tropsch synthesis products. *J Ind Eng Chem*. June 2018. doi:10.1016/J.JIEC.2018.05.044

18. Arora S, Prasad R. An overview on dry reforming of methane: strategies to reduce carbonaceous deactivation of catalysts. *RSC Adv*. 2016;6(110):108668-108688. doi:10.1039/C6RA20450C

19. Challiwala MS, Wilhite BA, Ghouri MM, Elbashir NO. Multidimensional modeling of a microfibrous entrapped cobalt catalyst Fischer-Tropsch reactor bed. *AIChE J*. 2018;64(5):1723-1731. doi:10.1002/aic.16053

20. Gu B, Khodakov AY, Ordomsky V V. Selectivity shift from paraffins to α-olefins in low temperature Fischer–Tropsch synthesis in the presence of carboxylic acids.

Chem Commun. 2018;54(19):2345-2348. doi:10.1039/C7CC08692J

21. Koo KY, Lee JH, Ho Jung U, Kim SH, Yoon WL. Combined H 2 O and CO 2 reforming of coke oven gas over Ca-promoted Ni/MgAl 2 O 4 catalyst for direct reduced iron production. 2015. doi:10.1016/j.fuel.2015.03.007

22. Pakhare D, Spivey J. A review of dry (CO 2) reforming of methane over noble metal catalysts. *Chem Soc Rev*. 2014;43:7813. doi:10.1039/c3cs60395d

23. Challiwala MS, Ghouri MM, Linke P, El-Halwagi MM, Elbashir NO. A combined thermo-kinetic analysis of various methane reforming technologies: Comparison with dry reforming. *J CO2 Util*. 2017;17:99-111. doi:10.1016/J.JCOU.2016.11.008

24. Noureldin MMB, Elbashir NO, El-Halwagi MM. Optimization and Selection of Reforming Approaches for Syngas Generation from Natural/Shale Gas. *Ind Eng Chem Res*. 2014;53(5):1841-1855. doi:10.1021/ie402382w

25. Pakhare D, Spivey J. A review of dry (CO_2) reforming of methane over noble metal catalysts. *Chem Soc Rev*. 2014;43(22):7813-7837. doi:10.1039/C3CS60395D

26. Bian Z, Das S, Wai MH, Hongmanorom P, Kawi S. A Review on Bimetallic Nickel-Based Catalysts for CO2 Reforming of Methane. *ChemPhysChem*. 2017;18(22):3117-3134. doi:10.1002/cphc.201700529

27. Kawi S, Kathiraser Y, Ni J, Oemar U, Li Z, Saw ET. Progress in Synthesis of Highly Active and Stable Nickel-Based Catalysts for Carbon Dioxide Reforming of Methane. *ChemSusChem*. 2015;8(21):3556-3575. doi:10.1002/cssc.201500390

28. Wang Y, Yao L, Wang S, Mao D, Hu C. Low-temperature catalytic CO 2 dry reforming of methane on Ni-based catalysts: A review. *Fuel Process Technol*. 2018;169(June 2017):199-206. doi:10.1016/j.fuproc.2017.10.007

29. Abdullah B, Abd Ghani NA, Vo DVN. Recent advances in dry reforming of methane over Ni-based catalysts. *J Clean Prod*. 2017;162:170-185. doi:10.1016/j.jclepro.2017.05.176

30. Jang W-J, Shim J-O, Kim H-M, Yoo S-Y, Roh H-S. A review on dry reforming of methane in aspect of catalytic properties. *Catal Today*. 2018:1-0. doi:10.1016/j.cattod.2018.07.032

31. Aramouni NAK, Touma JG, Tarboush BA, Zeaiter J, Ahmad MN. Catalyst design

for dry reforming of methane: Analysis review. *Renew Sustain Energy Rev*. 2018;82(December 2016):2570-2585. doi:10.1016/j.rser.2017.09.076

32. Pakhare D, Schwartz V, Abdelsayed V, et al. Kinetic and mechanistic study of dry (CO 2) reforming of methane over Rh-substituted La 2 Zr 2 O 7 pyrochlores. 2014. doi:10.1016/j.jcat.2014.04.023

33. Zhu YA, Chen D, Zhou XG, Yuan WK. DFT studies of dry reforming of methane on Ni catalyst. *Catal Today*. 2009;148(3-4):260-267. doi:10.1016/j.cattod.2009.08.022

34. Tomishige K, Chen Y-G, Fujimoto K. *Studies on Carbon Deposition in CO2 Reforming of CH4 overNickel–Magnesia Solid Solution Catalysts*. Vol 181.; 1999. http://www.idealibrary.comon. Accessed August 27, 2018.

35. Trimm DL. *Coke Formation and Minimisation during Steam Reforming Reactions*. Vol 37.; 1997. https://ac-els-cdn-com.ezproxy.library.tamu.edu/S092058619700014X/1-s2.0-S092058619700014X-main.pdf?_tid=03719725-c79c-4c3c-af93-b0bc0458578d&acdnat=1535354856_232f26433e5501507d0e403ccbd4fcc4. Accessed August 27, 2018.

36. Trimm DL. *Catalysts for the Control of Coking during Steam Reforming*. https://ac-els-cdn-com.ezproxy.library.tamu.edu/S0920586198004015/1-s2.0-S0920586198004015-main.pdf?_tid=4bc32656-557e-4b81-ab06-d2cf7c23d41b&acdnat=1535354989_1b2643402bce75130d7aa524356dfcdd. Accessed August 27, 2018.

37. Wang Z, Cao XM, Zhu J, Hu P. Activity and coke formation of nickel and nickel carbide in dry reforming: A deactivation scheme from density functional theory. *J Catal*. 2014;311:469-480. doi:10.1016/j.jcat.2013.12.015

38. Zhu X, Huo P, Zhang Y, Cheng D, Liu C. Structure and reactivity of plasma treated Ni/Al2O3 catalyst for CO2 reforming of methane. *Appl Catal B Environ*. 2008;81(1-2):132-140. doi:10.1016/J.APCATB.2007.11.042

39. Chung W-C, Chang M-B. Review of catalysis and plasma performance on dry reforming of CH4 and possible synergistic effects. *Renew Sustain Energy Rev*. 2016;62:13-31. doi:10.1016/J.RSER.2016.04.007

40. Bengaard HS, Nørskov JK, Sehested J, et al. Steam Reforming and Graphite Formation on Ni Catalysts. *J Catal*. 2002;209(2):365-384. doi:10.1006/JCAT.2002.3579

41. Chen D, Christensen KO, Ochoa-Fernández E, et al. Synthesis of carbon nanofibers: effects of Ni crystal size during methane decomposition. *J Catal*. 2005;229(1):82-96. doi:10.1016/J.JCAT.2004.10.017

42. Kim J-H, Suh DJ, Park T-J, Kim K-L. Effect of metal particle size on coking during CO2 reforming of CH4 over Ni–alumina aerogel catalysts. *Appl Catal A Gen*. 2000;197(2):191-200. doi:10.1016/S0926-860X(99)00487-1

43. Mo L, Saw ET, Du Y, et al. Highly dispersed supported metal catalysts prepared via in-situ self-assembled core-shell precursor route. *Int J Hydrogen Energy*. 2015;40(39):13388-13398. doi:10.1016/J.IJHYDENE.2015.07.105

44. Yang W, He D. Role of poly(N-vinyl-2-pyrrolidone) in Ni dispersion for highly-dispersed Ni/SBA-15 catalyst and its catalytic performance in carbon dioxide reforming of methane. *Appl Catal A Gen*. 2016;524:94-104. doi:10.1016/J.APCATA.2016.06.026

45. Shang Z, Li S, Li L, Liu G, Liang X. Highly active and stable alumina supported nickel nanoparticle catalysts for dry reforming of methane. *Appl Catal B Environ*. 2017;201:302-309. doi:10.1016/j.apcatb.2016.08.019

46. Han JW, Park JS, Choi MS, Lee H. Uncoupling the size and support effects of Ni catalysts for dry reforming of methane. *Appl Catal B Environ*. 2017;203:625-632. doi:10.1016/j.apcatb.2016.10.069

47. Mette K, Kühl S, Tarasov A, et al. High-Temperature Stable Ni Nanoparticles for the Dry Reforming of Methane. *ACS Catal*. 2016;6(10):7238-7248. doi:10.1021/acscatal.6b01683

48. Bian Z, Suryawinata IY, Kawi S. Highly carbon resistant multicore-shell catalyst derived from Ni-Mg phyllosilicate nanotubes@silica for dry reforming of methane. *Appl Catal B Environ*. 2016;195:1-8. doi:10.1016/J.APCATB.2016.05.001

49. Tian H, Li X, Zeng L, Gong J. Recent Advances on the Design of Group VIII Base-Metal Catalysts with Encapsulated Structures. 2015. doi:10.1021/acscatal.5b01221

50. Horlyck J, Lawrey C, Lovell EC, Amal R, Scott J. Elucidating the impact of Ni and Co loading on the selectivity of bimetallic NiCo catalysts for dry reforming of methane. *Chem Eng J*. 2018;352:572-580. doi:10.1016/J.CEJ.2018.07.009

51. Mohamedali M, Henni A, Ibrahim H. Recent Advances in Supported Metal Catalysts for Syngas Production from Methane. *ChemEngineering*. 2018;2(1):9.

doi:10.3390/chemengineering2010009

52. Nematollahi B, Rezaei M, Khajenoori M. Combined dry reforming and partial oxidation of methane to synthesis gas on noble metal catalysts. *Int J Hydrogen Energy*. 2011;36(4):2969-2978. doi:10.1016/J.IJHYDENE.2010.12.007

53. Foppa L, Silaghi MC, Larmier K, Comas-Vives A. Intrinsic reactivity of Ni, Pd and Pt surfaces in dry reforming and competitive reactions: Insights from first principles calculations and microkinetic modeling simulations. *J Catal*. 2016;343:196-207. doi:10.1016/j.jcat.2016.02.030

54. Tomishige K. Syngas production from methane reforming with CO2/H2O and O2 over NiO–MgO solid solution catalyst in fluidized bed reactors. *Catal Today*. 2004;89(4):405-418. doi:10.1016/J.CATTOD.2004.01.003

55. Li L, Zhou L, Ould-Chikh S, et al. Controlled Surface Segregation Leads to Efficient Coke-Resistant Nickel/Platinum Bimetallic Catalysts for the Dry Reforming of Methane. *ChemCatChem*. 2015;7(5):819-829. doi:10.1002/cctc.201402965

56. Lucci FR, Marcinkowski MD, Lawton TJ, Sykes ECH. H $_2$ Activation and Spillover on Catalytically Relevant Pt–Cu Single Atom Alloys. *J Phys Chem C*. 2015;119(43):24351-24357. doi:10.1021/acs.jpcc.5b05562

57. Ren J, Qin X, Yang JZ, et al. Methanation of carbon dioxide over Ni-M/ZrO<inf>2</inf> (M = Fe, Co, Cu) catalysts: Effect of addition of a second metal. *Fuel Process Technol*. 2015;137:204-211. doi:10.1016/j.fuproc.2015.04.022

58. Takanabe K, Nagaoka K, Nariai K, Aika K. Titania-supported cobalt and nickel bimetallic catalysts for carbon dioxide reforming of methane. *J Catal*. 2005;232(2):268-275. doi:10.1016/J.JCAT.2005.03.011

59. Budiman AW, Song S-H, Chang T-S, Shin C-H, Choi M-J. Dry Reforming of Methane Over Cobalt Catalysts: A Literature Review of Catalyst Development. *Catal Surv from Asia*. 2012;16(4):183-197. doi:10.1007/s10563-012-9143-2

60. Fan X, Liu Z, Zhu Y-A, et al. Tuning the composition of metastable CoxNiyMg100−x−y(OH)(OCH3) nanoplates for optimizing robust methane dry reforming catalyst. *J Catal*. 2015;330:106-119. doi:10.1016/J.JCAT.2015.06.018

61. Zhang J, Wang H, Dalai AK. Development of stable bimetallic catalysts for carbon dioxide reforming of methane. *J Catal*. 2007;249(2):300-310. doi:10.1016/J.JCAT.2007.05.004

62. Kim SM, Abdala PM, Margossian T, et al. Cooperativity and Dynamics Increase the Performance of NiFe Dry Reforming Catalysts. *J Am Chem Soc*. 2017;139(5):1937-1949. doi:10.1021/jacs.6b11487

63. Theofanidis SA, Batchu R, Galvita V V., Poelman H, Marin GB. Carbon gasification from Fe–Ni catalysts after methane dry reforming. *Appl Catal B Environ*. 2016;185:42-55. doi:10.1016/J.APCATB.2015.12.006

64. Xu L li, Wen H, Jin X, Bing Q ming, Liu J yao. DFT study on dry reforming of methane over Ni2Fe overlayer of Ni(1 1 1) surface. *Appl Surf Sci*. 2018;443:515-524. doi:10.1016/j.apsusc.2018.02.268

65. Theofanidis SA, Galvita V V., Poelman H, Marin GB. Enhanced Carbon-Resistant Dry Reforming Fe-Ni Catalyst: Role of Fe. *ACS Catal*. 2015;5(5):3028-3039. doi:10.1021/acscatal.5b00357

66. Kim SM, Abdala PM, Margossian T, et al. Cooperativity and Dynamics Increase the Performance of NiFe Dry Reforming Catalysts. 2017. doi:10.1021/jacs.6b11487

67. Xu L li, Wen H, Jin X, Bing Q ming, Liu J yao. DFT study on dry reforming of methane over Ni2Fe overlayer of Ni(1 1 1) surface. *Appl Surf Sci*. 2018;443(111):515-524. doi:10.1016/j.apsusc.2018.02.268

68. Pendem S, Mondal I, Shrotri A, Rao BS, Lingaiah N, Mondal J. Unraveling the structural properties and reactivity trends of Cu–Ni bimetallic nanoalloy catalysts for biomass-derived levulinic acid hydrogenation. *Sustain Energy Fuels*. 2018;2(7):1516-1529. doi:10.1039/C8SE00138C

69. Lo Faro M, Frontera P, Antonucci PL, Aricò AS. Ni-Cu based catalysts prepared by two different methods and their catalytic activity toward the ATR of methane. *Chem Eng Res Des*. 2015. doi:10.1016/j.cherd.2014.05.014

70. Zhang R, Guo X, Wang B, Ling L. Insight into the effect of CuNi(111) and FeNi(111) surface structure and second metal composition on surface carbon elimination by O or OH: A comparison study with Ni(111) surface. *J Phys Chem C*. 2015;119(25):14135-14144. doi:10.1021/acs.jpcc.5b03868

71. Hua B, Li M, Zhang W, Pu J, Chi B, Jian L. Methane On-Cell Reforming by Alloys Reduced from Ni0.5Cu0.5Fe2O4 for Direct-Hydrocarbon Solid Oxide Fuel Cells. *J Electrochem Soc*. 2014;161(4):F569-F575. doi:10.1149/2.097404jes

72. Vizcaíno AJ, Carrero A, Calles JA. Hydrogen production by ethanol steam

reforming over Cu-Ni supported catalysts. *Int J Hydrogen Energy*. 2007;32(10-11):1450-1461. doi:10.1016/j.ijhydene.2006.10.024

73. Kim H, Lu C, Worrell WL, Vohs JM, Gorte RJ. Cu-Ni Cermet Anodes for Direct Oxidation of Methane in Solid-Oxide Fuel Cells. *J Electrochem Soc*. 2002;149(3):A247. doi:10.1149/1.1445170

74. Kim H, Lu C, Worrell WL, Vohs JM, Gorte RJ. Cu-Ni Cermet Anodes for Direct Oxidation of Methane in Solid-Oxide Fuel Cells. *J Electrochem Soc*. 2002;149(3):A247. doi:10.1149/1.1445170

75. Misture ST, Mcdevitt KM, Glass KC, et al. From chip-in-a-lab to lab-on-a-chip: towards a single handheld electronic system for multiple application-specific lab-on-a-chip (ASLOC). *Cite this Catal Sci Technol*. 2014;5. doi:10.1039/c5cy00800j

76. Reshetenko T V, Avdeeva LB, Ismagilov ZR, Chuvilin AL, Ushakov VA. Carbon capacious Ni-Cu-Al2O3 catalysts for high-temperature methane decomposition. *Appl Catal A Gen*. 2003;247(1):51-63. doi:10.1016/S0926-860X(03)00080-2

77. Morán-Pineda M, Castillo S, López T, Gómez R, Cordero-Borboa, Novaro O. Synthesis, characterization and catalytic activity in the reduction of NO by CO on alumina–zirconia sol–gel derived mixed oxides. *Appl Catal B Environ*. 1999;21(2):79-88. doi:10.1016/S0926-3373(99)00010-7

78. Agnelli M, Mirodatos C. CO Hydrogenation on Nickel-Based Catalysts: Effects of Copper Addition. *J Catal*. 2000;192:204-214. doi:10.1006/jcat.2000.2828

79. Sharifi M, Haghighi M, Rahmani F, Karimipour S. Syngas production via dry reforming of CH4over Co- and Cu-promoted Ni/Al2O3-ZrO2nanocatalysts synthesized via sequential impregnation and sol-gel methods. *J Nat Gas Sci Eng*. 2014;21:993-1004. doi:10.1016/j.jngse.2014.10.030

80. Bonura G, Cannilla C, Frusteri F. Ceria–gadolinia supported NiCu catalyst: A suitable system for dry reforming of biogas to feed a solid oxide fuel cell (SOFC). *Appl Catal B Environ*. 2012;121-122:135-147. doi:10.1016/J.APCATB.2012.03.028

81. Rahemi N, Haghighi M, Akbar Babaluo A, Allahyari S, Fallah Jafari M. Syngas production from reforming of greenhouse gases CH 4 /CO 2 over Ni-Cu/Al 2 O 3 nanocatalyst: Impregnated vs. plasma-treated catalyst. *Energy Convers Manag*. 2014;84:50-59. doi:10.1016/j.enconman.2014.04.016

82. Wu T, Cai W, Zhang P, Song X, Gao L. Cu-Ni@SiO2alloy nanocomposites for

methane dry reforming catalysis. *RSC Adv*. 2013;3(46):23976-23979. doi:10.1039/c3ra43203c

83. Liu H, Zhang R, Yan R, et al. Insight into CH 4 dissociation on NiCu catalyst: A first-principles study there is serious carbon deposition on NiCu/MgO-Al 2 O 3 in CO 2 reforming of methane [. *Appl Surf Sci*. 2012;258:8177-8184. doi:10.1016/j.apsusc.2012.05.017

84. Liu H, Wang B, Fan M, et al. Study on carbon deposition associated with catalytic CH 4 reforming by using density functional theory. 2013. doi:10.1016/j.fuel.2013.06.022

85. An W, Zeng XC, Turner CH. First-principles study of methane dehydrogenation on a bimetallic Cu/Ni(111) surface. *Cit J Chem Phys*. 2009;131(111):134704. doi:10.1063/1.3254383

86. Wang M, Fu Z, Yang Z. The carbon-tolerance mechanism of Ni-based alloy with coinage metals. *Phys Lett Sect A Gen At Solid State Phys*. 2013;377(34-36):2189-2194. doi:10.1016/j.physleta.2013.05.054

87. Tavares MT, Alstrup I, Bernardo CA, Rostrup-Nielsen JR. *Carbon Formation and CO Methanation on Silica-Supported Nickel and Nickel-Copper Catalysts in CO H 2 Mixtures*. Vol 158.; 1996. https://core.ac.uk/download/pdf/55605070.pdf. Accessed August 19, 2018.

88. Chen H-W, Wang C-Y, Yu C-H, Tseng L-T, Liao P-H. Carbon dioxide reforming of methane reaction catalyzed by stable nickel copper catalysts. *Catal Today*. 2004;97(2-3):173-180. doi:10.1016/J.CATTOD.2004.03.067

89. Rafiee A, Rajab Khalilpour K, Milani D, Panahi M. Title: Trends in CO 2 conversion and utilization: A review from process systems Perspective. 2018. doi:10.1016/j.jece.2018.08.065

90. Biraben JN. An essay concerning mankind's demographic evolution. *J Hum Evol*. 1980;9(8):655-663. doi:10.1016/0047-2484(80)90099-8

91. Perea-Moreno M-A, Hernandez-Escobedo Q, Perea-Moreno A-J, Perea-Moreno M-A, Hernandez-Escobedo Q, Perea-Moreno A-J. Renewable Energy in Urban Areas: Worldwide Research Trends. *Energies*. 2018;11(3):577. doi:10.3390/en11030577

92. Gao Y, Jiang J, Meng Y, Yan F, Aihemaiti A. A review of recent developments in hydrogen production via biogas dry reforming. *Energy Convers Manag*.

2018;171:133-155. doi:10.1016/j.enconman.2018.05.083

93. Centi G, Quadrelli EA, Perathoner S. Catalysis for CO2 conversion: a key technology for rapid introduction of renewable energy in the value chain of chemical industries. *Energy Environ Sci*. 2013;6(6):1711. doi:10.1039/c3ee00056g

94. Jason M. Ginsburg †, Juliana Piña ‡, Tarek El Solh § and, Hugo I. de Lasa* †. Coke Formation over a Nickel Catalyst under Methane Dry Reforming Conditions: Thermodynamic and Kinetic Models. 2005. doi:10.1021/IE0496333

95. Sholl DS, Steckel JA. *Density Functional Theory : A Practical Introduction*. Wiley; 2009. https://www.wiley.com/en-us/Density+Functional+Theory%3A+A+Practical+Introduction-p-9780470373170. Accessed November 20, 2018.

96. Kohn W, Sham LJ. *Physical Review: Self-Consistent Equations Including Exchange and Correlation Effects**. http://users.wfu.edu/natalie/s15phy752/lecturenote/KohnPhysRev.140.A1133.pdf. Accessed December 8, 2018.

97. Bickelhaupt FM, Baerends EJ. Kohn-Sham Density Functional Theory: Predicting and Understanding Chemistry. In: Wiley-Blackwell; 2007:1-86. doi:10.1002/9780470125922.ch1

98. Kresse G, Furthmiiller B ' J. *Efficiency of Ab-Initio Total Energy Calculations for Metals and Semiconductors Using a Plane-Wave Basis Set*. Vol 6.; 1996. https://ac-els-cdn-com.ezproxy.library.tamu.edu/0927025696000080/1-s2.0-0927025696000080-main.pdf?_tid=e3d03892-c3db-4281-bc4c-d8e2999faed2&acdnat=1536770056_83116e6f9c9ce254fe25b05e26d525cc. Accessed September 12, 2018.

99. Kresse G, Furthmüller J. Efficient iterative schemes for *ab initio* total-energy calculations using a plane-wave basis set. *Phys Rev B*. 1996;54(16):11169-11186. doi:10.1103/PhysRevB.54.11169

100. Perdew JP, Burke K, Ernzerhof M. *Generalized Gradient Approximation Made Simple*.; 1996. https://journals-aps-org.ezproxy.library.tamu.edu/prl/pdf/10.1103/PhysRevLett.77.3865. Accessed September 12, 2018.

101. Monkhorst HJ, Pack JD. *Special Points for Brillonin-Zone Integrations**. Vol 13.; 1976. https://journals-aps-org.ezproxy.library.tamu.edu/prb/pdf/10.1103/PhysRevB.13.5188. Accessed

September 12, 2018.

102. Methfessel M, Paxton AT. *High-Precision Sampling for Brillouin-Zone Integration in Metals*. Vol 40. https://journals-aps-org.ezproxy.library.tamu.edu/prb/pdf/10.1103/PhysRevB.40.3616. Accessed September 12, 2018.

103. Henkelman G, Jónsson H, Jó H. Improved tangent estimate in the nudged elastic band method for finding minimum energy paths and saddle points. *Cit J Chem Phys*. 2000;113:2082. doi:10.1063/1.1323224

104. Henkelman G, Jónsson H, Jó H. A dimer method for finding saddle points on high dimensional potential surfaces using only first derivatives Improved tangent estimate in the nudged elastic band method for finding minimum energy paths and saddle points Optimization methods for finding minimum energy paths A dimer method for finding saddle points on high dimensional potential surfaces using only first derivatives. *Cit J Chem Phys*. 1999;111:14106. doi:10.1063/1.480097

105. Fan C, Zhu Y, Yang M, Sui ZJ, Zhou X, Chen D. DFT-assisted microkinetic analysis of methane dry reforming on Ni catalyst DFT-assisted microkinetic analysis of methane dry reforming on Ni catalyst. 2015;(May):1-12. doi:10.1021/acs.iecr.5b00563

106. Henkelman G, Arnaldsson A, Jónsson H. Theoretical calculations of CH 4 and H 2 associative desorption from Ni"111…: Could subsurface hydrogen play an important role? 2006. doi:10.1063/1.2161193

107. Sharia O, Holzgrafe J, Park N, Henkelman G. Rare event molecular dynamics simulations of plasma induced surface ablation. *J Chem Phys*. 2014;141:74706. doi:10.1063/1.4892841

108. Research Computing @ TAMUQ. Getting started with RAAD2 - Research Computing @ TAMUQ. https://rc-docs.qatar.tamu.edu/index.php/Raad2_getstarted. Accessed January 14, 2019.

109. Wei J, Iglesia E. Isotopic and kinetic assessment of the mechanism of reactions of CH 4 with CO 2 or H 2 O to form synthesis gas and carbon on nickel catalysts. *J Catal*. 2004;224:370-383. doi:10.1016/j.jcat.2004.02.032

110. Michaelides A, Hu P. *Methyl Chemisorption on Ni(111) and CMHMM Multicentre Bonding: A Density Functional Theory Study*. Vol 437.; 1999. www.elsevier.nl/locate/susc. Accessed November 14, 2018.

111. Zhu Y-A, Dai Y-C, Chen D, Yuan W-K. First-principles calculations of CH 4 dissociation on Ni(1 0 0) surface along different reaction pathways. *J Mol Catal A Chem*. 2007;264:299-308. doi:10.1016/j.molcata.2006.09.043

112. Wei J, Iglesia E. Isotopic and kinetic assessment of the mechanism of reactions of CH 4 with CO 2 or H 2 O to form synthesis gas and carbon on nickel catalysts. *J Catal*. 2004;224:370-383. doi:10.1016/j.jcat.2004.02.032

113. Bradford MCJ, Vannice MA. Catalytic reforming of methane with carbon dioxide over nickel catalysts II. Reaction kinetics. *Appl Catal A Gen*. 1996;142(1):97-122. doi:10.1016/0926-860X(96)00066-X

114. Heiland W. Charge exchange processes and surface chemistry. *Surf Sci*. 1991;251-252:942-946. doi:10.1016/0039-6028(91)91129-L

115. Pérez-Hernández R, Gutiérrez-Martínez A, Espinosa-Pesqueira ME, Estanislao ML, Palacios J. Effect of the bimetallic Ni/Cu loading on the ZrO<inf>2</inf>support for H<inf>2</inf>production in the autothermal steam reforming of methanol. *Catal Today*. 2015;250. doi:10.1016/j.cattod.2014.08.009

116. Jørgensen M. Microkinetic Modeling of Nanoparticle Catalysis using Density Functional Theory. *PhD thesis*. 2017.

117. Liu C, Ye J, Jiang J, Pan Y. Progresses in the Preparation of Coke Resistant Ni-based Catalyst for Steam and CO2 Reforming of Methane. *ChemCatChem*. 2011;3(3):529-541. doi:10.1002/cctc.201000358

118. Ray D, Ghosh S, Tiwari AK. Controlling Heterogeneous Catalysis of Water Dissociation Using Cu−Ni Bimetallic Alloy Surfaces: A Quantum Dynamics Study. *J Phys Chem A*. 2018;122:5698-5709. doi:10.1021/acs.jpca.8b03237

119. Foppa L, Silaghi M-C, Larmier K, Comas-Vives A. Intrinsic reactivity of Ni, Pd and Pt surfaces in dry reforming and competitive reactions: Insights from first principles calculations and microkinetic modeling simulations. *J Catal*. 2016;343:196-207. doi:10.1016/J.JCAT.2016.02.030

120. Jørgensen M. Microkinetic Modeling of Nanoparticle Catalysis using Density Functional Theory. 2017.

121. Sautet P, Schrödinger E. Computational Catalysis. 2013. doi:10.1039/9781849734905

122. Pounds AJ. Introduction to Quantum Mechanics in Chemistry (Ratner, Mark A.;

Schatz, George C.). *J Chem Educ*. 2002;79(4):434. doi:10.1021/ed079p434

123. Hammer B, Norskov JK. Theoretical Surface Science and Catalysis — Calculations and Concepts. *Adv Catal*. 2000;45:71-129. doi:http://dx.doi.org/10.1016/S0360-0564(02)45013-4

124. Haas P, Tran F, Blaha P. Calculation of the lattice constant of solids with semilocal functionals. 2009. doi:10.1103/PhysRevB.79.085104

125. Maslov MM, Openov LA, Podlivaev AI. *On the Vineyard Formula for the Pre-Exponential Factor in the Arrhenius Law*. https://arxiv.org/ftp/arxiv/papers/1406/1406.3621.pdf. Accessed December 7, 2018.

126. Henkelman G, Uberuaga BP, Jó H. *A Climbing Image Nudged Elastic Band Method for Finding Saddle Points and Minimum Energy Paths*.; 2000. http://theory.cm.utexas.edu/henkelman/pubs/henkelman00_9901.pdf. Accessed December 8, 2018.

APPENDIX

I. DFT (Density Functional Theory)

The total energy of a system of atoms is calculated using the stationary Schrödinger equation:

$$\hat{H}\,\Psi = E\Psi \tag{16}$$

Where the many-body Hamiltonian $\hat{H}$ can be written:

$$\hat{H} = \hat{H}_{eZ} + \hat{H}_{ee} + \hat{H}_{ZZ} \tag{17}$$

The expression includes contributions from electron-nuclei interactions (eZ), electron-electron interactions (ee), and nuclei-nuclei interactions (ZZ). The corresponding Schrödinger equation does not allow an analytical solution for more than one electron, and must be solved by approximations such as Born-Oppenheimer approximation which is sufficient to deal with the electronic part of the Hamiltonian[95].

The 1st H-K theorem states that the ground state electronic density (ρ) uniquely determines the external potential (V_{ext}). This implies that ρ also determines the ground state Ψ of the many body problems.The second HK theorem defines the variational energy as a functional of ρ:

$$E_v[\rho] = \langle \Psi[\rho] | \check{T} + \check{U}_{ee} | \Psi[\rho] \rangle + \int \rho(r)\, v_{ext}(r)\, dr \tag{18}$$

$$E\,[\{\Psi\,i\}] = E_{known}[\{\Psi\,i\}] + E_{XC}[\{\Psi\,i\}] \qquad (19)$$

where v_{ext} is the external potential, $\check{T}$ is the kinetic energy operator for the electrons[120]. To simplify, the energy functional at Eq (19) from HK can be rewritten as

$$E_{\text{known}}[\{\psi_i\}] = \frac{h^2}{m}\sum_i \int \psi_i^* \nabla^2 \psi_i d^3r + \int V(\mathbf{r}) n(\mathbf{r})\, d^3r + \frac{e^2}{2}\int\int \frac{n(\mathbf{r}) n(\mathbf{r}')}{|\mathbf{r} \quad \mathbf{r}'|}\, d^3r\, d^3r' + E_{\text{ion}}.$$

The terms on E_{known} are, in order, the electron kinetic energies, the Coulomb interactions between the electrons and the nuclei, the Coulomb interactions between pairs of electrons, and the Coulomb interactions between pairs of nuclei[96]. The other term in the complete energy functional, $E_{XC}[\{\Psi_i\}]$,is the exchange–correlation functional, and it is defined to include all the quantum mechanical effects that are not included in the "known" terms[97].

The self interaction is unphysical, and the correction for it is one of several effects that are lumped together into the final potential in the Kohn–Sham equations, V_{XC}, which defines exchange and correlation contributions to the single electron equations. V_{XC} can formally be defined as a "functional derivative" of the exchange–correlation energy:

$$V_{XC}(r) = \delta E_{XC}(r) / \delta n(r) \quad (20)$$

The only remaining unknown quantity here is the exchange-correlation energy, which determines the accuracy of DFT[121,122,97].

II. Exchange correlation energy approximations

The approximation of the exchange-correlation functional is a major concern when it comes to the accuracy of DFT[97].

Two kinds of exchange-correlation approximation is the Local Density Approximation (LDA) and Generalized Gradient Approximation GGA. In LDA, the exchange-correlation is approximated by considering the inhomogeneous electron gas as being locally homogeneous, thus applying the exchange-correlation hole of the homogeneous electron gas[96]. GGA approximation improves over LDA by taking into account the gradient of the density[100]. Multiple GGA functionals have been developed throughout time, and one popular choice is the Perdew-Burke-Ernzerhof (PBE) functional. Another GGA functional derived from PBE is the ***revised PBE functional*** of Hammer et al. (RPBE), which is *optimized for chemisorptions,* which is of unique importance for microkientic modeling[123,124].

III. Energy barriers with NEB (Nudged Elastic Band)

Nudged elastic band (NEB) is a method to find the Minimum Energy Path (MEP) between an initial state and final state, and NEB is also used to identify the transition state.

To initialize a NEB calculation, the initial and final atomic positions are determined from adsorption calculations. The resulting atomic configurations are called images, and the distance between the images are described by a reaction coordinate r. Structural optimization is done on each image, which is connected to the other images by modifying the force component parallel to the MEP. The total force on each image is decomposed in parallel and perpendicular components as:

$$F = F_{//} + F_{\perp} = -kr + F_{\perp} \quad (21)$$

where k is a spring constant. Typically, the transition state is not found without releasing the highest energy image from all spring forces, and reversing the true parallel force component. As a result, the image climbs up the MEP to the true transition state. This procedure is called the Climbing Image method.

IV. Rate constant calculation

The temperature dependence of the rate k of one or another thermally activated process in solids or atomic clusters (diffusion, decomposition, isomerization, etc.) is often described by the harmonic approximation to TST (hTST) can typically be used in studies of diffusion and reactions in crystals or at crystal surfaces. Accordingly, the rate constant k^{hTST} (T) can be calculated by:.....

$$k^{hTST}(T) = A \exp(-E_a/K_B T) \quad (22)$$

where T is the temperature, K_B is the Boltzmann constant, Ea is the activation energy (the minimum energy required to be transferred to the system to overcome an energy barrier on the corresponding reaction path), and A is the frequency factor with dimension of s^{-1} [125,126].

The frequency factor *A* is calculated according to the Vineyard formula, which for an *N*-atom cluster with zero values of the total momentum and the total angular momentum has the form

$$A = \frac{\prod_{i=1}^{3N-6} vi}{\prod_{i=1}^{3N-7} v'\mathrm{i}} \tag{23}$$

where v_i are the eigenfrequencies of vibrations of the cluster in the state corresponding to the minimum of the potential energy Epot for all 3N – 6 normal coordinates, and v_i, v_i` are the frequencies of vibrations at the saddle point corresponding to the maximum of $E_{pot}$ for one normal coordinate and to the minimum for all the other coordinates (since one of the 3N – 6 frequencies $v_i$` is imaginary, it is not included in the denominator of the expression for A[126].Similary,the Zero-Point energy correction can be calculated as[37]:

$$E_{ZPE}=\sum_i \frac{hvi}{2} \tag{24}$$

V. Input and output files:

The following **Figure 33**, **Figure 34, Figure 35** and **Figure 36** shows DFT input calculation parameters and VASP^{TM} output for the Ni_2Cu over-layered Ni (111) slab.

```
#General
  System = C+H-Cu-Ni(111)-TopNi 3X3 4 layers in Z-direction - (7 layers) of vacuum
  ISTART = 0
  ICHARG = 2
#Electronic relaxation
  ENCUT  = 400
  ISPIN  = 2
  NELM   = 50
  NELMIN = 6
  NELMDL = 10
  EDIFF  = 1.0E-04
  ALGO   =  Fast
  IDIPOL = 3
#Ionic relaxation
  EDIFFG = -0.01
  NSW    = 50
  IBRION = 3 #CNEB
  ISIF   = 2
#DOS related
  SIGMA  = 0.2
  ISMEAR = 1
  LORBIT = 11
# My Additions
   PREC  = HIGH
   GGA   =  RP
# Parallelization
   #LPLANE = .TRUE.
   KPAR = 6
   NCORE  = 48
   #LSCALU = .FALSE.
   #NSIM   = 4
#CNEB
   POTIM = 0
   IMAGES = 8
   SPRING = -5.0 # eV/A2
   IOPT = 3
   LCLIMB =.TRUE.
#OPTIMIZER Parameters
   MAXMOVE = 0.2  #Maximum allowed step size for translation
   TIMESTEP = 0.1 #Dynamical time step
#Stop writing heavy files
"INCAR" 45L, 974C
```

Figure 33 Sample input files for cNEB calculations showing all input settings.

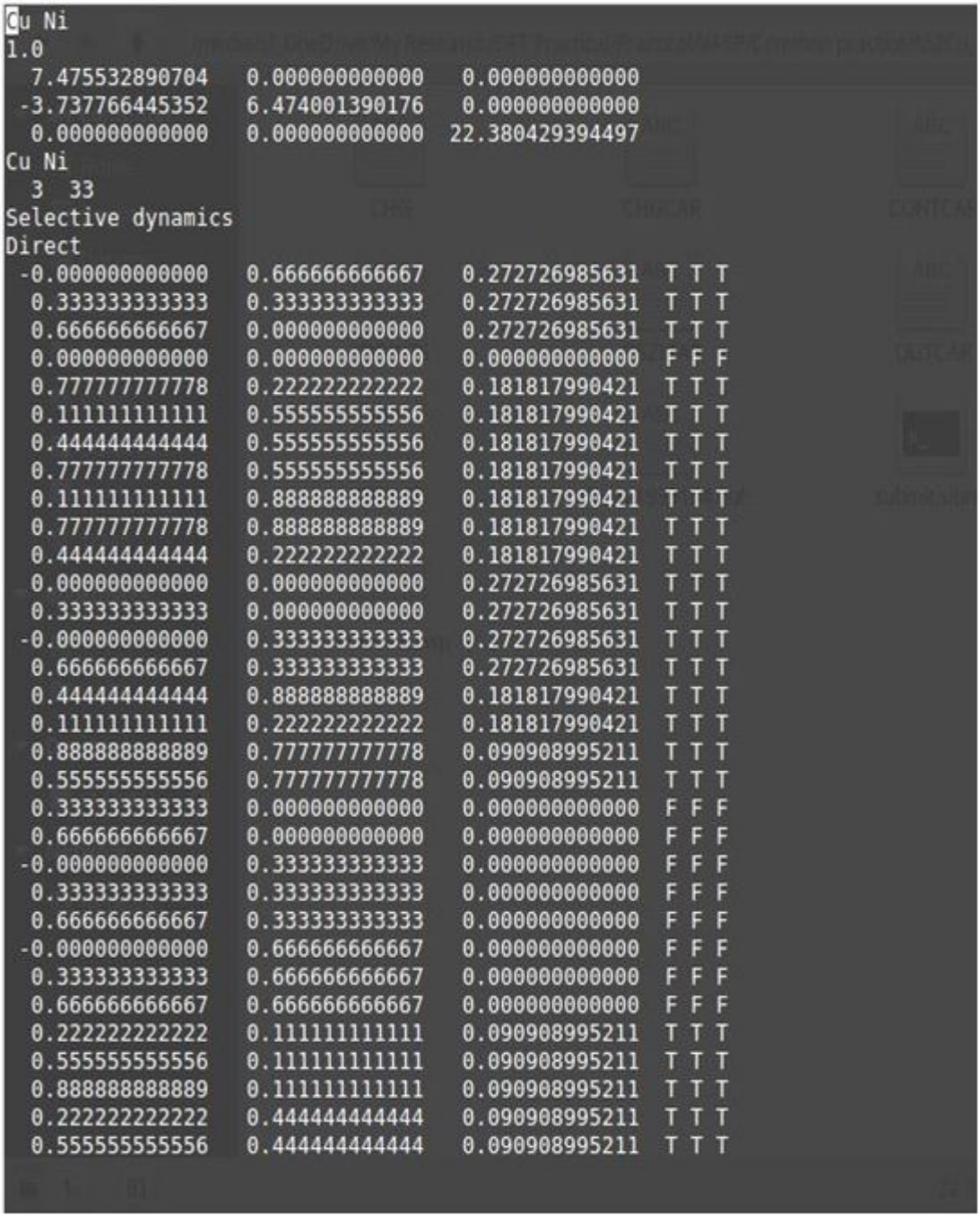

```
Cu Ni
1.0
  7.475532890704   0.000000000000   0.000000000000
 -3.737766445352   6.474001390176   0.000000000000
  0.000000000000   0.000000000000  22.380429394497
Cu Ni
  3  33
Selective dynamics
Direct
 -0.000000000000   0.666666666667   0.272726985631  T T T
  0.333333333333   0.333333333333   0.272726985631  T T T
  0.666666666667   0.000000000000   0.272726985631  T T T
  0.000000000000   0.000000000000   0.000000000000  F F F
  0.777777777778   0.222222222222   0.181817990421  T T T
  0.111111111111   0.555555555556   0.181817990421  T T T
  0.444444444444   0.555555555556   0.181817990421  T T T
  0.777777777778   0.555555555556   0.181817990421  T T T
  0.111111111111   0.888888888889   0.181817990421  T T T
  0.777777777778   0.888888888889   0.181817990421  T T T
  0.444444444444   0.222222222222   0.181817990421  T T T
  0.000000000000   0.000000000000   0.272726985631  T T T
  0.333333333333   0.000000000000   0.272726985631  T T T
 -0.000000000000   0.333333333333   0.272726985631  T T T
  0.666666666667   0.333333333333   0.272726985631  T T T
  0.444444444444   0.888888888889   0.181817990421  T T T
  0.111111111111   0.222222222222   0.181817990421  T T T
  0.888888888889   0.777777777778   0.090908995211  T T T
  0.555555555556   0.777777777778   0.090908995211  T T T
  0.333333333333   0.000000000000   0.000000000000  F F F
  0.666666666667   0.000000000000   0.000000000000  F F F
 -0.000000000000   0.333333333333   0.000000000000  F F F
  0.333333333333   0.333333333333   0.000000000000  F F F
  0.666666666667   0.333333333333   0.000000000000  F F F
 -0.000000000000   0.666666666667   0.000000000000  F F F
  0.333333333333   0.666666666667   0.000000000000  F F F
  0.666666666667   0.666666666667   0.000000000000  F F F
  0.222222222222   0.111111111111   0.090908995211  T T T
  0.555555555556   0.111111111111   0.090908995211  T T T
  0.888888888889   0.111111111111   0.090908995211  T T T
  0.222222222222   0.444444444444   0.090908995211  T T T
  0.555555555556   0.444444444444   0.090908995211  T T T
```

Figure 34 Sample POSCAR file shows the position of Ni and Cu atoms in Ni (111) slab.

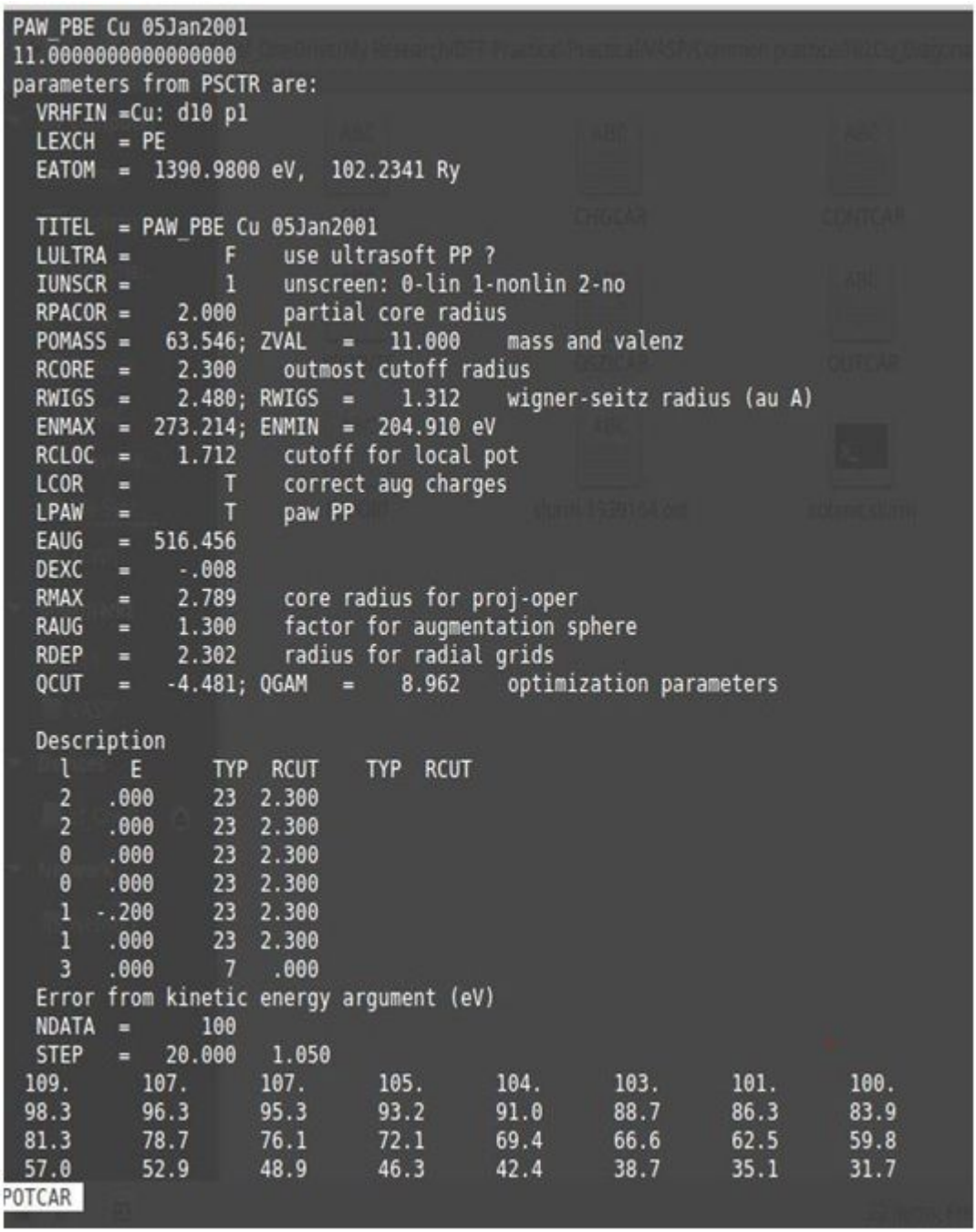

Figure 35 Sample POTCAR file shows the PAW of Cu.

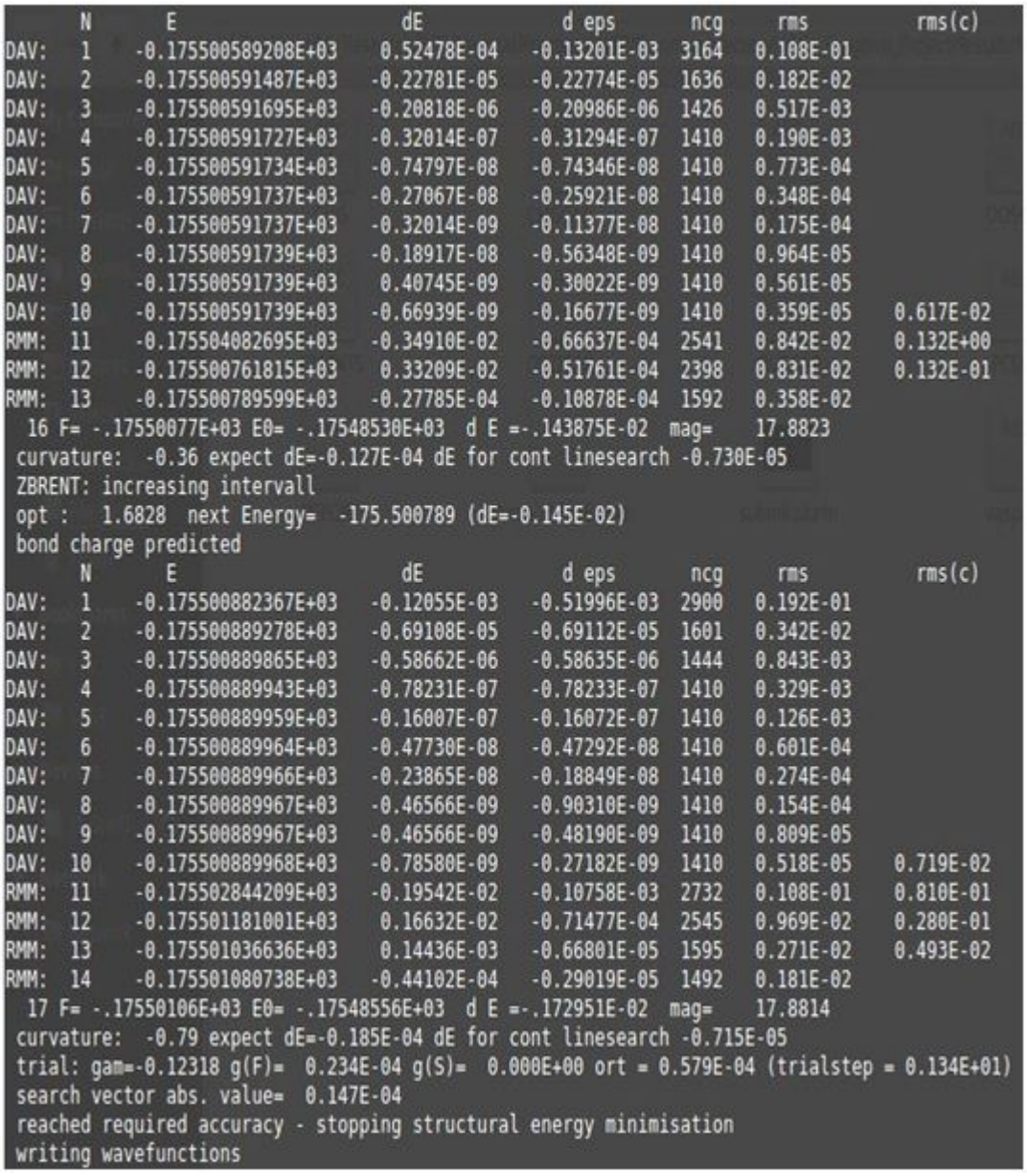

```
      N       E                     dE             d eps       ncg     rms          rms(c)
DAV:   1    -0.175500589208E+03    0.52478E-04   -0.13201E-03  3164   0.108E-01
DAV:   2    -0.175500591487E+03   -0.22781E-05   -0.22774E-05  1636   0.182E-02
DAV:   3    -0.175500591695E+03   -0.20818E-06   -0.20986E-06  1426   0.517E-03
DAV:   4    -0.175500591727E+03   -0.32014E-07   -0.31294E-07  1410   0.190E-03
DAV:   5    -0.175500591734E+03   -0.74797E-08   -0.74346E-08  1410   0.773E-04
DAV:   6    -0.175500591737E+03   -0.27067E-08   -0.25921E-08  1410   0.348E-04
DAV:   7    -0.175500591737E+03   -0.32014E-09   -0.11377E-08  1410   0.175E-04
DAV:   8    -0.175500591739E+03   -0.18917E-08   -0.56348E-09  1410   0.964E-05
DAV:   9    -0.175500591739E+03    0.40745E-09   -0.30022E-09  1410   0.561E-05
DAV:  10    -0.175500591739E+03   -0.66939E-09   -0.16677E-09  1410   0.359E-05    0.617E-02
RMM:  11    -0.175504082695E+03   -0.34910E-02   -0.66637E-04  2541   0.842E-02    0.132E+00
RMM:  12    -0.175500761815E+03    0.33209E-02   -0.51761E-04  2398   0.831E-02    0.132E-01
RMM:  13    -0.175500789599E+03   -0.27785E-04   -0.10878E-04  1592   0.358E-02
  16 F= -.17550077E+03 E0= -.17548530E+03  d E =-.143875E-02  mag=    17.8823
 curvature:  -0.36 expect dE=-0.127E-04 dE for cont linesearch -0.730E-05
 ZBRENT: increasing intervall
 opt :   1.6828  next Energy=  -175.500789 (dE=-0.145E-02)
 bond charge predicted
      N       E                     dE             d eps       ncg     rms          rms(c)
DAV:   1    -0.175500882367E+03   -0.12055E-03   -0.51996E-03  2900   0.192E-01
DAV:   2    -0.175500889278E+03   -0.69108E-05   -0.69112E-05  1601   0.342E-02
DAV:   3    -0.175500889865E+03   -0.58662E-06   -0.58635E-06  1444   0.843E-03
DAV:   4    -0.175500889943E+03   -0.78231E-07   -0.78233E-07  1410   0.329E-03
DAV:   5    -0.175500889959E+03   -0.16007E-07   -0.16072E-07  1410   0.126E-03
DAV:   6    -0.175500889964E+03   -0.47730E-08   -0.47292E-08  1410   0.601E-04
DAV:   7    -0.175500889966E+03   -0.23865E-08   -0.18849E-08  1410   0.274E-04
DAV:   8    -0.175500889967E+03   -0.46566E-09   -0.90310E-09  1410   0.154E-04
DAV:   9    -0.175500889967E+03   -0.46566E-09   -0.48190E-09  1410   0.809E-05
DAV:  10    -0.175500889968E+03   -0.78580E-09   -0.27182E-09  1410   0.518E-05    0.719E-02
RMM:  11    -0.175502844209E+03   -0.19542E-02   -0.10758E-03  2732   0.108E-01    0.810E-01
RMM:  12    -0.175501181001E+03    0.16632E-02   -0.71477E-04  2545   0.969E-02    0.280E-01
RMM:  13    -0.175501036636E+03    0.14436E-03   -0.66801E-05  1595   0.271E-02    0.493E-02
RMM:  14    -0.175501080738E+03   -0.44102E-04   -0.29019E-05  1492   0.181E-02
  17 F= -.17550106E+03 E0= -.17548556E+03  d E =-.172951E-02  mag=    17.8814
 curvature:  -0.79 expect dE=-0.185E-04 dE for cont linesearch -0.715E-05
 trial: gam=-0.12318 g(F)=  0.234E-04 g(S)=  0.000E+00 ort = 0.579E-04 (trialstep = 0.134E+01)
 search vector abs. value=  0.147E-04
 reached required accuracy - stopping structural energy minimisation
 writing wavefunctions
```

Figure 36 Sample Output File show the slab energy after required accuracy is reached.